

# Preparation and manipulation of molecules for fundamental physics tests

M. R. Tarbutt, J. J. Hudson, B. E. Sauer, and E. A. Hinds  
*Centre for Cold Matter, The Blackett Laboratory,  
Imperial College London, London SW7 2AZ, UK*

## I. INTRODUCTION

Atoms and atomic ions have long held a place at the very heart of precision measurement and metrology. For example, the second is defined in terms of the Cs hyperfine structure interval, the Rydberg constant is measured by spectroscopy of atomic hydrogen and the ratio of electron to proton mass is known from the oscillation frequencies of trapped atomic ions. The importance of atoms in this field lies partly in the detailed understanding that we have of atomic structure but also in the technical capabilities that exist for preparing and manipulating atoms and ions. In recent years, both the computational methods for understanding molecules more fully and the experimental methods for producing and controlling them have advanced enormously. This has led to a surge of interest in using molecules for precision measurements, especially where they offer new properties that are not available from atoms and atomic ions. For example, the rotational, vibrational and electronic structures within a molecule offer a wider range of co-existing frequencies than one finds in atomic systems. Moreover, polar diatomic molecules have a built-in cylindrical symmetry, whilst more complex molecules can have a handedness - structural conformations that atoms cannot offer. In this chapter, we discuss some applications of molecules to current problems in precision measurement and we outline recent technical advances that make some of these applications possible.

## II. TESTING INVARIANCE PRINCIPLES

### A. Do fundamental constants vary in time?

Recent measurements have shown that the expansion of the universe is accelerating, requiring the Einstein equations of cosmology to have a “dark energy” term, which was previously assumed to be zero[1]. This surprise, together with the ongoing search for a quantum theory of gravity, has led theorists to question some of the most basic assumptions in our physical model of the universe, including the assumption that the constants of nature are indeed constant over time.

In atomic and molecular physics, two of these constants are particularly important. They are the fine structure constant  $\alpha$ , and the electron-to-proton mass ratio  $\mu = m_e/m_p$ . The Rydberg energy  $Ry$  sets the gross scale of electronic binding energy. Relative to this, the fine structure splittings are characteristically smaller by

the factor  $\alpha^2$  and the hyperfine structure is smaller again by a further factor of order  $\mu$ , since  $\mu$  relates the magnetic moment of the nucleus to that of the electron. Consequently, it is possible to search for a variation of  $\alpha$  by comparing fine and gross structure at two different times. Similarly the variation of  $\mu$  can be deduced from a further comparison of the hyperfine structure with one of the other energy scales. Molecules bring an important new dimension to this search [2] by adding two more energy scales: vibrational energy of order  $Ry\sqrt{m_e/M}$  and rotational energy of order  $Ry(m_e/M)$ , where  $M$  is the reduced nuclear mass. Uzan [3] has recently reviewed both the theoretical framework and the experimental tests for variable constants.

So far, the most productive experimental method has been to study astronomical spectra, which permit measurements of  $\Delta\alpha/\alpha$  and  $\Delta\mu/\mu$ , typically with a precision of 1 part in  $10^5$ , over enormous time intervals of order 10 Gyr, giving uncertainties of order  $10^{-15}/\text{year}$  in the average value of  $\dot{\alpha}/\alpha$  or  $\dot{\mu}/\mu$ . At this level, some observations seem to hint at a variation[4, 5], while others do not [6, 7]. In order to interpret the astronomical data one needs to know the sensitivity of each transition to  $\alpha$  and  $\mu$ , which requires input both from laboratory data and from numerical modelling. Using  $\text{H}_2$  in this way, Reinhold *et al.* [5] have found an average variation over 12 Gyr of  $\dot{\mu}/\mu = (1.7 \pm 0.5) \times 10^{-15}/\text{year}$ , which differs from zero by  $3.4\sigma$ . The ground state  $\Lambda$ -doublet of OH has also been observed at large redshift. The transition frequency for this interval relative to its hyperfine structure yields information on both  $\alpha$  and  $\mu$  [7]. When compared with the structure of OH today, these astrophysical measurements looking back 6.5 Gyr indicate with  $2\sigma$  confidence that  $\dot{\mu}/\mu < 2.1 \times 10^{-15}/\text{year}$  on average and is consistent with zero. A laboratory experiment using a molecular decelerator to make slow OH [8] (there is more on deceleration in Sec. V) has recently improved our knowledge of these transition frequencies in the current epoch. This will allow further improvement in the astronomical data to yield an even better determination of  $\dot{\mu}$  and  $\dot{\alpha}$  in the near future. Another frequency with high sensitivity to  $\mu$  is the inversion splitting of  $\text{NH}_3$  due to tunnelling. Analysis of quasar absorption spectra, comparing the inversion line to rotational transitions, has placed a limit  $\dot{\mu}/\mu = (-1 \pm 3) \times 10^{-16}\text{yr}^{-1}$  [10] on the variation of  $\mu$ . This leaves the astronomical measurements in an intriguing but uncertain state. Are there systematic errors yet to be uncovered? Do the constants vary or not, and if they do, is the variation irregular in time or perhaps non-uniform in space?

There is a good prospect that laboratory measure-

ments can help to clarify the situation. Although the time intervals available for comparison are short - years rather than giga-years - this method provides a promising alternative because recently developed frequency comb methods can link optical frequencies directly to the Cs standard, giving an absolute frequency accuracy below one part in  $10^{15}$  [11]. Even higher accuracy, approaching one part in  $10^{17}$  is becoming available in measuring relative frequencies [12]. Several molecular experiments of this type are now under way. It has been suggested [13] that the cold, trapped molecular ions  $\text{H}_2^+$  or  $\text{HD}^+$  could be used to measure changes in  $\mu$  to a precision of 1 part in  $10^{15}$ . A second laboratory-based proposal [14] is to compare the inversion splitting measured in a slow, cold fountain of  $\text{ND}_3$  to an atomic reference. A third project is in progress to measure vibrational transitions in  $\text{SF}_6$  [15].

### B. Testing fundamental symmetries

The electromagnetic forces that bind atoms and molecules together obey Maxwell's equations and the Dirac equation, as synthesised in quantum electrodynamics. This field theory has three important symmetry properties: it is invariant under space inversion (parity, P) charge conjugation (exchange of particles and antiparticles, C) and time reversal (T). These symmetries have profound experimental consequences. For example, the eigenstates of atoms and molecules have definite parity (unless there are degenerate conformations), leading to selection rules for radiative transitions. For similar reasons, atoms and molecules cannot have a permanent electric dipole moment (EDM) (barring degenerate conformations). For example, the well known EDM of ammonia is not permanent because the nitrogen atom tunnels back and forth at a frequency set by the splitting of the two opposite-parity field-free states. Of course, this splitting is small, and therefore it takes only a modest electric field to induce a dipole moment.

For some years it was surmised that all interactions possess these symmetries, but an experiment in 1956 [16] showed that weak interactions violate parity, as seen by the fact that radioactive decay particles are emitted with a large left-right asymmetry. Within a decade, an experiment on the decay of kaon particles showed that strong interactions are also not symmetrical, having a small asymmetry under the combined operation CP [17]. There is a theorem for the type of theories used to describe particle interactions (local, Lorenz-invariant field theories) that they must be invariant under the triple reflection CPT. Since CP symmetry is broken, this theorem seems to indicate that T symmetry is also broken at the same level. These symmetry (and asymmetry) properties have played an important role in developing the standard model of particle interactions, which describes electromagnetic, weak, and strong interactions.

The discovery of CP-violation led to a fascinating ques-

tion. Is it possible that particles, atoms and molecules do have permanent electric dipole moments after all? This would require interactions that violate both P and T, but we know that the weak and strong interactions together can do that. As it happens, the standard model, with its standard P and T violation, predicts exceedingly small EDM values. This is the result of a fortuitous cancellation, which comes about from the simplicity of the standard model. The pressing issue today is to discover what lies beyond the standard model. In order to understand more clearly the origin of mass and in order to accommodate a quantum theory of gravity it seems very likely that there are more particles than the standard collection. Such an increase in complexity immediately leads to the prediction that particles, atoms and molecules have EDMs much larger than the standard model values. They are still very small, but they are no longer too small to measure. Therefore, the search for a permanent electric dipole moment of an atom or molecule is really the search for particle physics beyond the standard model. Molecules are beginning to play a central part in this search.

The EDM  $d_{e,p,n}\vec{\sigma}$  of an electron, proton or neutron, is necessarily aligned along the spin direction  $\vec{\sigma}$  of the particle. In essence, an EDM measurement in an atom or molecule involves polarizing the system with an applied external electric field and searching for the interaction  $\eta d_x \vec{\sigma} \cdot \vec{E}$  between the electronic or nuclear EDM and the polarised atom/molecule. Schiff's theorem [18] states that  $\eta = 0$  if the atom/molecule is made of point particles bound by electrostatic forces. In other words, the electronic or nuclear EDM does not see the applied field because it is shielded out by the other charged particles. This theorem is important for its loopholes: nuclei are not point particles and the electric dipole interaction is not screened when the electrons are relativistic. Consequently,  $\eta$  is not zero if the atom/molecule is well chosen [19, 20]. For example the best measurement of the proton EDM comes from a measurement on TlF molecules [21], where the large size of the Tl nucleus ends up giving  $\eta \sim 1$  for the nuclear spin EDM interaction. The upper limit on the neutron EDM is known both directly, from measurements on free neutrons [22], and indirectly, from nuclear spin measurements on Hg atoms [23].

For electron EDM measurements, as opposed to neutron or proton measurements,  $\eta$  can be much larger than 1 if the electron moves relativistically within the atom or molecule. For example, the Tl atom is very sensitive to the electron EDM  $d_e$ , with  $\eta = -585$ . Currently, the best limit on the electron EDM is derived from such an experiment on Tl atoms [24]. The effective interaction  $\eta d_e \vec{\sigma} \cdot \vec{E}$  is linear in  $\vec{E}$  because the polarisation of the atom is proportional to the applied electric field. This polarisation is small for atoms in laboratory strength fields because it derives from the mixing of higher electronic states induced by the field and these are typically  $10^{15}$  Hz higher in energy. By contrast, a heavy polar molecule is polarised by mixing rotational states, which are typically

only 10 GHz away, giving five orders of magnitude more polarisability and a correspondingly larger  $\eta$ . The polarisation due to rotational mixing stops increasing once the molecule is largely aligned with the field and then  $\eta\vec{E}$  approaches a saturated value. For the YbF molecule, this value is an enormous 26 GV/cm [25].

A group at Imperial College, including the authors of this article, are currently in the process of measuring  $d_e$  using the YbF molecule [26]. In comparison with the Tl atom, this molecule gives roughly 500 times more EDM interaction energy, whereas the interaction with magnetic fields is essentially the same. Since stray magnetic fields constitute the primary source of systematic errors this is a significant advantage. However, Tl beams have much better statistical noise because they are much more intense than YbF beams. At present the gain in sensitivity is roughly offset by the loss in signal, and the YbF experiment is taking data at a level of precision similar to the Tl experiment [26]. In the new era of high-precision molecular beam measurements that we are discussing here, the need for brighter, colder, slower sources is a recurring theme that we address again in the next section.

Other molecular approaches to EDM measurement are also being pursued. The group of DeMille is aiming to measure the electron EDM in a metastable  $\Omega$ -doublet of PbO [27] using vapour in a cell. The group of Cornell is investigating the possibility of using trapped molecular ions [28], among which  $\text{HfF}^+$  appears to be a promising candidate. There is also a proposal to make a dense sample of some radical such as YbF and to measure the magnetisation induced by aligning the electron EDMs in an applied electric field [29].

We turn now to parity violation without T violation. This is very well understood in the standard model of particle physics as a normal feature of weak interactions. It is also well established in atomic physics through the measurements on Cs atoms [30]. However, it remains a fascinating topic in the context of molecular physics, partly because it has not been observed in molecules but mainly because chirality plays such an important role in chemistry. The weak interaction is predicted to alter the energy spectrum between enantiomers of chiral molecules. Indeed, it is still a subject of debate whether the parity violation of weak interactions has played any role in establishing the chirality of the biochemistry in living organisms [31, 32]. The most intensively studied species are the methyl halides, CH-XYZ, where X, Y, Z are three different halogens [33]. The largest effect is predicted to be a 50.8 mHz shift in the C-F stretching mode between left and right handed versions of CHFBrI. By contrast, the best experimental results [34] reach a precision of 50Hz. It appears that cold trapped molecules will be necessary to measure weak interactions in these systems. Much larger enantiomer shifts, in the range of several Hz, have recently been predicted for some rhenium and osmium complexes [35] and these may be observable using supersonic beams.

There is also nuclear physics interest in parity violation

because it plays a role in nuclear structure. A particularly interesting possibility is that weak interactions in nuclei can induce an anapole moment, a P-odd multipole that produces no external field and corresponds in lowest order to a toroidal flow of current within the nucleus. An experiment is underway at Yale University to measure the anapole moment of the  $^{137}\text{Ba}$  nucleus using BaF molecules [36].

The last symmetry we mention here is Lorentz invariance, which has been a central plank of 20th century physics and has so far shown no indication of being violated in nature. Even so, it is possible that new physics, associated with quantum gravity at the Planck energy scale, could lead to very small violations of Lorentz invariance in the laboratory [37]. For example, there might be a change in the energy of an atom depending on the orientation of its spin relative to some preferred direction, such as its velocity in the rest frame of the universe. Very sensitive experiments of this sort have already been performed using a variety of atomic clocks [38]. More recently, it has been pointed out that diatomic molecules provide a new way to investigate Lorentz invariance by orienting the internuclear axis of the molecule relative to the proposed preferred direction. The symmetry violation could then be read out as a shift in the energy, bond length, vibration frequency, or rotation frequency [39]. Sensitivities for  $\text{H}_2$  and HD and their cations have been calculated in [39]. The authors conclude that an experiment to measure the ground state rovibrational transitions can improve limits on some elements of the Lorentz tensor  $c_{\mu\nu}$  [40] by an order of magnitude. It is very likely that other more polar molecules could be convenient to use and that this area will develop as techniques for preparing, cooling and trapping molecules progress further.

In the rest of this chapter, we discuss the production and detection of intense molecular beams, particularly of heavy polar radicals. We also describe methods of using pulsed molecular beams to map fields in the beamline and to detect interactions through the quantum coherences. Finally, we describe advances in slowing heavy polar molecules with a view to trapping them. These rather practical issues are the key points to be addressed if molecules are to fulfill the fantastic promise that we have just outlined for elucidating exotic fundamental physics.

### III. BEAMS OF COLD POLAR RADICALS

All molecular beams must begin with a source. A good source will provide a large number of molecules in the quantum state of interest for the experiment. In most cases, the molecules need to be prepared in a single low-lying rotational state, and so the temperature of the molecules should ideally be smaller than the rotational energy spacing, typically 1 K or less. Pulsed sources of cold molecules, very narrowly distributed in both position and velocity, offer many advantages. They can be

prepared with very high intensity without imposing an excessive gas load on the vacuum system, they can be used to map the electromagnetic field along the beamline with high resolution and precision, they allow quantum coherences to be prepared and manipulated with great accuracy, and they can be slowed down in a Stark decelerator to increase the coherence times. In this section, we concentrate on the formation and detection of cold, pulsed beams of the radical molecules that are typically required for measuring the P and T violating interactions discussed above.

Supersonic expansion is a very common technique for producing cold molecular beams [41, 42]. A high pressure gas expands through a nozzle into a vacuum chamber, acquiring a high centre-of-mass velocity but very narrow velocity distribution. The translational degrees of freedom are cooled, as are the internal degrees of freedom of the molecules. While the first beams were continuous, the method was later extended by using pulsed valves with short opening times [43, 44]. The individual pulses could then be made very intense, without the gas load becoming excessive. Often, the molecules of interest have low vapour pressure, and need to be formed by laser ablation or electric discharge techniques. This is usually done immediately outside the nozzle of the pulsed valve, or inside an extended nozzle, where the density of carrier gas is high enough to entrain a useful fraction of the molecules produced [45]. In our laboratory, we have used laser ablation to produce cold beams of YbF [46], CaF and LiH molecules [47]. In all cases, we detect our pulsed beams using time-resolved, Doppler-free, laser induced fluorescence (LIF). This detection method is very well suited for precision measurements where high sensitivity, high frequency resolution, and good beam diagnostics are all required.

### A. Apparatus

The typical experimental setup is illustrated in Fig. 1. A solenoid valve emits short pulses of the carrier gas [48], which is usually Ar, Kr or Xe, into a vacuum chamber maintained at pressures below  $10^{-4}$  mbar. The central part of the gas pulse passes through a skimmer, of diameter 1-2 mm, placed 50-100 mm downstream of the source, and into the high vacuum region where the pressure is below  $10^{-7}$  mbar. A fast ionization gauge placed on the axis of the beamline can be used to ensure good alignment. Using two such gauges, one immediately outside the nozzle and the other much further downstream, the initial width, the speed and the translational temperature of the gas pulses can all be measured. The shortest gas pulses we obtain with this valve have a full width at half maximum (FWHM) of  $81 \mu\text{s}$  [46]. In an ideal supersonic expansion from a reservoir at temperature  $T_0$ , the carrier gas approaches a terminal velocity

$$v_T = \sqrt{(2k_B T_0/m)\gamma/(\gamma-1)}, \quad (1)$$

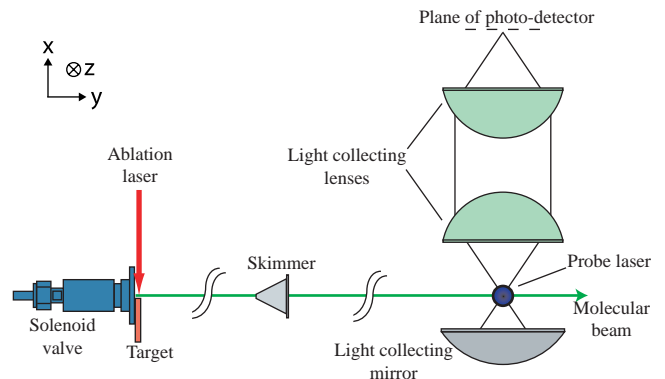


FIG. 1: Typical experimental setup for producing pulsed beams of cold polar radicals, and detecting them by laser induced fluorescence. Not to scale.

where  $\gamma$  is the specific heat ratio,  $5/3$  for an ideal monatomic gas, and  $m$  is the mass of an atom of the carrier gas. Our measurements using a range of carrier gases and temperatures show that the true speed of the carrier gas is 5-15% faster than  $v_T$ .

A suitable target, placed outside the nozzle of the valve, is ablated using light from a Q-switched laser. To ensure minimal disruption of the gas pulse, the target is thin in the direction of the gas-jet, typically 2-5 mm. The resulting ablation plume can usually be observed by eye. It is forward peaked along the normal to the target, which is usually perpendicular to the direction of the beamline. Some of the atoms and molecules in the plume become entrained in the high density carrier gas, thereby cooling to temperatures and speeds that approach those of the carrier gas. The target may either contain all the precursors needed to form the molecules of interest, or some of the precursors can be added to the carrier gas. For example, we have produced beams of YbF either by ablating pure Yb and mixing  $\text{SF}_6$  into the carrier gas, or by ablating a pressed target containing a mixture of Yb and  $\text{AlF}_3$  powders. The former method is slightly simpler to realise, but both methods work equally well. We typically use ablation pulses of 5-10 ns duration, focussed to a spot-size of 1-2 mm. Under these conditions, the optimal ablation energy is in the range 10-50 mJ.

A photomultiplier, placed some distance (typically 10-150 cm) downstream, detects the molecules by means of cw-laser-induced fluorescence. The laser is directed at right angles to the molecular beam in order to minimise the Doppler shift and is tuned to a strong molecular transition. The transit time of the molecules through the laser beam is typically  $5 - 10 \mu\text{s}$ , giving this method high temporal resolution. The width of the fluorescence excitation spectrum is usually greater than the transit time limit, being typically 20-50 MHz. This comes from a combination of the residual Doppler width, due to the angular distribution of the molecules, and the natural lifetime of the excited state. Such high spectral resolution is typically needed in order to resolve the hyperfine

structure and hence to permit coherent state manipulation and readout at rf frequencies. The fluorescence detection method is very sensitive. If the detection efficiency is  $\epsilon$  (assumed  $\ll 1$ ) and there are  $N$  molecules per shot passing through the detector area in a time interval  $w'$ , then the shot noise limited signal-to-noise ratio for a single shot will be  $s : n = \epsilon N / \sqrt{bw' + \epsilon N}$ , where  $b$  is the background rate of detected photons. In a good detection setup,  $bw' \approx 1$  and  $\epsilon$  is in the range 1-10%. Taking  $\epsilon = 0.02$  as a typical value, we find that the signal-to-noise ratio per shot is 1 when  $N = 81$  molecules.

## B. Translational temperature and source size

Figure 2 shows the time-of-flight profiles of ground state YbF molecules recorded by two separate LIF detectors placed 340 mm and 1300 mm from the pulsed source. The background laser scatter is lower at the downstream detector. In this experiment, the molecules were produced by ablating pure Yb just outside the nozzle of the solenoid valve which was pressurized to 4 bar with a mixture of Ar(98%) and SF<sub>6</sub>(2%). The probe laser was tuned to excite the  $F = 1$  hyperfine component of the  $X^2\Sigma^+(v'' = 0) - A^2\Pi_{1/2}(v' = 0) Q(0)$  transition. There are four contributions to the spread of arrival times - (i) the temporal spread of the molecules produced at the source, (ii) their spatial spread at the source, (iii) the forward velocity distribution in the pulse and (iv) the temporal resolution of the detector. The last of these is usually small enough to be neglected.

The flux of molecules with speeds in the interval from  $v$  to  $v + dv$  is usually taken to be  $f(v) dv = Av^3 \exp(-M(v - v_0)^2/2k_B T) dv$ , where  $M$  is the mass,  $T$  is the translational temperature,  $v_0$  is the central velocity and  $A$  is a normalizing constant. Consider those molecules born in the source at time  $t_s$  with initial position  $s$  along the beam axis. In the LIF detector, placed a distance  $L$  away from the source, these molecules produce a time-dependent signal

$$h(t, t_s, s) = \frac{A(L-s)^4}{(t-t_s)^5} \exp\left(\frac{-Mv_0^2}{2k_B T} \frac{(t_0 - s/v_0 - t + t_s)^2}{(t-t_s)^2}\right), \quad (2)$$

where  $t_0 = L/v_0$ . As we shall soon see, both the temporal width and spatial width of the source are small,  $t_s \ll t_0$  and  $s \ll L$ . Furthermore, at typical detection distances, the range of arrival times is much smaller than the mean arrival time, and it is valid to set  $t \approx t_0$  everywhere except in the numerator of the exponent. With these approximations, Eq. (2) simplifies to

$$h(t, t_s, \rho) \approx A \frac{L^4}{t_0^5} \exp\left(-\frac{4 \ln 2 (t - t_0 - t_s - \rho)^2}{w^2}\right), \quad (3)$$

where  $\rho = -s/v_0$ , and  $w = (8 \ln 2 k_B T t_0^2 / (Mv_0^2))^{1/2}$  is the temporal width (FWHM) of the pulse due to the thermal spread of forward velocities.

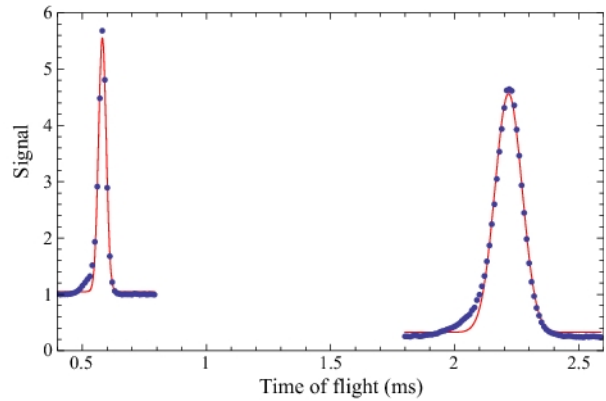


FIG. 2: Time of flight profiles of ground state YbF recorded by two laser induced fluorescence detectors, situated 340 mm and 1300 mm from the source. The lines are Gaussian fits to the two datasets.

The signal at the detector is obtained by integrating over the temporal and spatial distributions present in the source. We do not know these distributions, but we can hope to obtain a measure of their characteristic widths. In this spirit, we assume that the source emits the normalised distribution

$$g(t_s, \rho) = \frac{4 \ln 2}{\pi \Delta_{t_s} \Delta_\rho} \exp\left(\frac{-4 \ln 2 t_s^2}{\Delta_{t_s}^2}\right) \exp\left(\frac{-4 \ln 2 \rho^2}{\Delta_\rho^2}\right). \quad (4)$$

Then, the detector records the signal

$$\begin{aligned} h(t) &= \iint h(t, t_s, \rho) g(t_s, \rho) dt_s d\rho \\ &= A \frac{L^4}{t_0^5} \frac{w}{w'} \exp\left(-4 \ln 2 \frac{(t - t_0)^2}{w'^2}\right) \end{aligned} \quad (5)$$

where the pulse width  $w'^2 = w^2 + \Delta_{t_s}^2 + \Delta_\rho^2$  includes the broadening due to the distribution of positions and times where molecules are first formed.

As shown by the Gaussian fits in Fig. 2, the recorded profiles are well described by the model except in the high velocity tails. The long tail, indicating a hotter component in the beam, is a common feature of our source when optimized for maximum signal and minimum shot-to-shot fluctuation; it can be removed by re-optimizing for low temperature. By using two well-separated detectors, the translational temperature can be obtained. It is

$$T = \frac{Mv_0^2}{8 \ln 2 k_B T} \frac{w_2'^2 - w_1'^2}{t_2^2 - t_1^2}, \quad (6)$$

where  $w_1'$ ,  $w_2'$ ,  $t_1$  and  $t_2$  are the widths (FWHM) and central arrival times obtained from Gaussian fits to the downstream and upstream data. For the data shown, the

speed is  $v_0 = 586$  m/s and the temperature is  $T = 4.8$  K. The use of two detectors allows an unambiguous determination of the temperature, whereas a single detector alone sets only an upper limit. However, if the detector is far from the source, that upper limit can be very close to the true temperature. For this data, the downstream detector alone provides an upper limit that is just 1.3% higher than the measured 4.8 K.

Having measured the temperature, we can also extract from the data upper limits on the initial temporal and spatial spreads at the source. For the data shown, these are  $\Delta t_s < 14.5 \mu\text{s}$  and  $v_0 \Delta \rho < 8.5$  mm. In separate experiments, using a dual ablation technique, we have measured  $\Delta t_s \approx 5 \mu\text{s}$  [47].

### C. Molecular flux

We consider next how to determine the absolute flux of molecules from the LIF signal. The detector counts the flux of photons, and we wish to convert this to a flux of molecules by knowing the mean number of fluorescent photons emitted from each molecule. To find this, we model the molecule as a 3-level system and use rate equations. Every molecule starts out in level 1 and passes through the laser, which excites the resonance between levels 1 and 2. The excitation rate is  $R$ , as is the rate of stimulated emission. It is directly proportional to the laser intensity,  $I$ , and depends on the detuning  $\delta = \omega_L - \omega_{12}$  of the laser angular frequency,  $\omega_L$ , from the molecular resonance frequency,  $\omega_{12}$ . Taking the optical Bloch equations in the limit where the coherences have reached a steady state, one finds that

$$R = \frac{\Gamma/2}{(1 + 4\delta^2/\Gamma^2)} \frac{I}{I_s}, \quad (7)$$

where  $\Gamma$  is the spontaneous decay rate of level 2,  $I_s = \epsilon_0 c \hbar^2 (\Gamma/2)^2 / D^2$  is the saturation intensity, and  $D$  is the matrix element of the dipole operator connecting levels 1 and 2. Level 1 is stable, while level 2 decays with rate  $r\Gamma$  to level 1, and rate  $(1-r)\Gamma$  to level 3 which represents all the other states in the molecule. The rates for excitation or decay out of level 3 are negligible.

We solve the rate equations to find the number of molecules in level 2 as a function of time,  $N_2(t)$ . Integrating  $\Gamma N_2(t)$  over the laser-molecule interaction time,  $\tau$ , we find the number of fluorescent photons emitted per molecule to be

$$n_p = \frac{R\Gamma}{R_+ - R_-} \left( \frac{e^{-R_+\tau} - 1}{R_+} - \frac{e^{-R_-\tau} - 1}{R_-} \right), \quad (8)$$

where

$$R_{\pm} = R + \Gamma/2 \pm \sqrt{R^2 + rR\Gamma + \Gamma^2/4}. \quad (9)$$

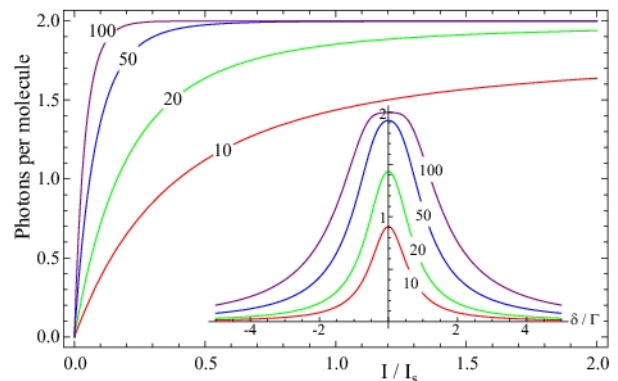


FIG. 3: Number of fluorescent photons per molecule,  $n_p$ , when the branching ratio for returning to the initial state is  $r = 0.5$ . In the main graph,  $n_p$  is plotted versus the intensity,  $I/I_s$ , for  $\Gamma\tau = 10, 20, 50, 100$ . The inset shows for each case how  $n_p$  varies with the laser detuning,  $\delta/\Gamma$ , when  $I = I_s/3$ .

In the limit where  $R_+\tau \gg 1$  and  $R_-\tau \gg 1$ ,  $n_p$  acquires its asymptotic value  $n_{p,\text{max}} = 1/(1-r)$ ; this is simply the sum of the obvious geometric series,  $n_{p,\text{max}} = \sum_{N=0}^{\infty} r^N$ . For good detection efficiency, we would like to ensure that  $n_p$  reaches its maximum possible value, and so we should examine how easily this limit is reached. If, as is usual, level 2 is an electronically excited state with an allowed electric dipole transition,  $\Gamma$  will typically exceed  $10^7 \text{ s}^{-1}$ . The interaction time,  $\tau$ , is usually greater than  $1 \mu\text{s}$ , and so we are in the limit  $\Gamma\tau \gg 1$ . If we suppose that the laser excitation is weak, in the sense that  $R \ll \Gamma$  (or, equivalently,  $I \ll I_s$ ), we get

$$n_p = \frac{1 - e^{-R(1-r)\tau}}{1 - r} \quad (\Gamma\tau \gg 1, R \ll \Gamma). \quad (10)$$

The limit  $n_p = 1/(1-r)$  is reached once  $R(1-r)\tau \gg 1$ , at which point the fluorescence signal saturates. Note that it is usual for  $\Gamma\tau$  to be greater than 100, and that for molecules, it is rare to have  $r$  close to 1. It follows that the above ‘saturation’ condition can easily be met, even when  $I \ll I_s$  – the fluorescence signal saturates for laser intensities well below  $I_s$  because the interaction time is very long compared to the time required for the molecule to reach level 3, the dark state.

Figure 3 shows the value of  $n_p$  as a function of  $I/I_s$  for four different values of  $\Gamma\tau$  with  $r = 0.5$ . The maximum value of  $n_p$  is 2, and in the case of  $\Gamma\tau = 100$ ,  $n_p$  is within 1% of this limit at  $I = I_s/4$ . At lower values of  $\Gamma\tau$ , the asymptotic value is lowered and more intensity is required to reach it. For example, when  $\Gamma\tau = 10$ ,  $n_p$  has an asymptotic value of 1.84 and is 78% of this value when  $I = I_s$ . The saturation process described here also leads to a type of power broadening of the spectral line when the laser frequency is scanned. An increase in laser intensity increases the fluorescence in the wings of the resonance more than at the centre of the resonance, and so the line is broadened. This is seen in the inset to Fig. 3,

where the lineshape is plotted for the various values of  $\Gamma\tau$ , in the case where  $r = 0.5$  and  $I = I_s/3$ .

If the decay rate of the excited state happens to be small, it is possible that the system will be in the opposite limit,  $\Gamma\tau \ll 1$ . In that case, even if  $R \gg \Gamma$ , the mean number of photons scattered by each molecule will be much smaller than 1, and independent of  $r$ . In fact, in this limit, Eq. (8) becomes

$$n_p = \Gamma(2R\tau + e^{-2R\tau} - 1)/(4R) \quad (\Gamma\tau \ll 1, R \gg \Gamma). \quad (11)$$

The fluorescence saturates to the value  $\Gamma\tau/2$  at high laser intensities.

Finally, it is interesting to consider the case where the interaction time is long ( $R\tau \gg 1$ ,  $\Gamma\tau \gg 1$ ) and  $r$  is very close to 1 so that each molecule has the possibility of scattering a large number of photons. Then, Eq. (8) reduces to the familiar atomic physics result,

$$n_p = \frac{R\Gamma\tau}{2R + \Gamma} = \frac{\Gamma\tau}{2} \frac{I/I_s}{1 + I/I_s + 4\delta^2/\Gamma^2}. \quad (12)$$

The on-resonance fluorescence now saturates to  $\Gamma\tau/2$  when the condition  $I \gg I_s$  is met.

Returning to the determination of the molecular flux, we write the total number of photons detected per shot as

$$p = \frac{1}{L^2} \iint N(x, z) \epsilon(x, z) n_p(x, z) dx dz, \quad (13)$$

where  $N(x, z)$ ,  $\epsilon(x, z)$  and  $n_p(x, z)$  are the number of molecules per steradian in the quantum state of interest, the detection efficiency and the number of fluorescent photons per molecule, all in the interval  $dx dz$  around the point  $(x, z)$  in the plane of detection. To determine the molecular flux as accurately as possible, the detection area should be defined by placing a small aperture on the molecular beam axis, slightly upstream of the detector, to block all but a small portion of the molecular beam. Similarly, the probe laser should be collimated and prepared with a top-hat intensity distribution in the  $x$  direction. Then  $N$  and  $\epsilon$  will be constant over the detection area. The value of  $n_p$  will be independent of  $x$ , but because of the Doppler shift, it remains a sensitive function of  $z$ , particularly if the degree of saturation is not high. Under these conditions, Eq. (13) reduces to

$$p = \frac{HN\epsilon}{L} \int n_p(\theta) d\theta, \quad (14)$$

where  $\theta = z/L$  and  $H$  is the height (along  $x$ ) of the detection area. The integral is straightforward to calculate by substituting the Doppler shift  $\delta = 2\pi v_0 \theta / \lambda$  into Eq. (7) and then using Eqs. (8) and (9) (the probe laser, of wavelength  $\lambda$ , is assumed to be on resonance). The

calculation requires some knowledge of  $r$ ,  $\Gamma$  and  $I_s$ , but provided the detection is in the saturated regime, rough estimates will suffice since the result becomes rather insensitive to  $\Gamma$  and  $I_s$ , and also to  $r$  if  $r$  is small, as is often the case.

For the detection setup shown in Fig. 1, the total detection efficiency is

$$\epsilon = (\Omega_l/4\pi) \sum_i q_i (1 + \mathcal{R}(\lambda_i)) T_l(\lambda_i)^2 \chi(\lambda_i). \quad (15)$$

Here,  $q_i$  is the fraction of fluorescent photons in the emission line whose wavelength is  $\lambda_i$ ,  $\mathcal{R}$ ,  $T_l$  and  $\chi$  are the wavelength-dependent mirror reflectivity, lens transmission, and photodetector quantum efficiency and  $\Omega_l$  is the solid angle subtended by the light-gathering lens. If windows and filters are present in the setup, their transmissions need to be included too.

By measuring the value of  $p$  and performing the above calculations, the flux of molecules in the detected quantum state can be determined. With careful measurements, an uncertainty below 50% should be possible. For the cold YbF molecules produced in our laboratory, the flux is measured to be  $1.4 \times 10^9$  ground state molecules per steradian per shot, when the carrier gas is argon [46].

#### D. Rotational temperature

The rotational temperature of the molecules can be determined by scanning the laser frequency and recording the rotational spectrum. When the rotational temperature is  $T_r$ , the intensity of a rotational line in the spectrum is proportional to  $N(J)\epsilon(J)n_p(J)$ , where  $N(J) = (2J + 1) \exp(-BJ(J + 1)/k_B T_r)$  is the relative number of molecules in the rotational state  $J$ ,  $B$  is the rotational constant, and  $\epsilon(J)$ ,  $n_p(J)$  express the  $J$ -dependence of the detection efficiency and the number of scattered photons per molecule. Usually, the efficiency  $\epsilon$  is almost independent of  $J$ . In many cases this is also true of  $n_p$ , making it easy to extract the rotational temperature from the relative line intensities once a few rotational lines have been measured. A more accurate temperature determination must take into account the variation of the matrix elements with  $J$ . For example, in  $^1\Sigma - ^1\Sigma$  transitions, the  $M_J$ -averaged value of  $D^2$  in the R-lines is proportional to  $(J + 1)/(2J + 1)$ , which decreases from 1 to 1/2 as  $J$  goes from 0 to  $\infty$ . For the P-lines, by contrast,  $D^2 \propto J/(2J + 1)$ , which increases from 0 to 1/2. Since this variation of the matrix elements generally affects both the excitation rate  $R$  and the branching ratio  $r$ , it influences the value of  $n_p(J)$  in both the saturated and unsaturated regimes. In the saturated regime, where  $n_p \simeq 1/(1 - r)$ , the variation of  $n_p$  with  $J$  is strongest if  $r$  happens to be close to 1.

In our lab, we have measured rotational temperatures of YbF, CaF and LiH beams. For the first two, the rotational temperatures are usually very close to the trans-

lational temperatures (typically in the range 1-5 K) [46]. For LiH we measure rotational temperatures considerably higher than the translational temperature [47].

### E. Source noise

The flux of molecules obtained from these sources is subject to shot-to-shot fluctuations, as well as having a slow drift (mostly downward). The time scale for the slow drift is typically  $10^4 - 10^5$  shots on a given spot of the target. We usually attach the target to the rim of a large disk, typically 20 cm in diameter, which we rotate incrementally as each target spot becomes exhausted. In this way, the lifetime of a target is of order  $10^7$  shots. The ability to run the source continuously for long periods of time is very important for precision measurements. A second essential requirement is that the shot-to-shot fluctuations be small, since they can contribute directly to the noise in the experiment. In measuring the electron electric dipole moment using cold YbF molecules, our detector records approximately 3000 photons per shot, with a corresponding  $\sqrt{N}$  photon shot-noise limit of 2%. Source fluctuations should ideally be kept below that level, but this proves rather difficult to achieve; when optimized, the short-time-scale fluctuations of our source are typically 2-3%.

## IV. COHERENT MANIPULATION OF INTERNAL STATES

### A. Stark and Zeeman shifts of the hyperfine states

In section III C, we discussed the excitation of higher electronic states using laser light to drive optical dipole transitions. The interaction was strongly damped by spontaneous emission from the upper level; indeed, the molecules were detected by means of the scattered photons. In this section, we consider some ways to manipulate the hyperfine sublevels within the ground state of the molecule. In contrast to optical transitions, the coherences between these ground-state levels are not radiatively damped because the spontaneous transition rates are very low for transition frequencies in the sub-GHz range. The control of these coherences provides a basis for exceedingly high precision measurements of electric and magnetic fields and for measurements such as that of the electron EDM.

In order to be concrete in our discussion, let us take the simple case illustrated in Fig. 4, of two hyperfine levels,  $F = 1$  and  $F = 0$ , such as one finds in a diatomic  $X^2\Sigma(N = 0)$  molecule with nuclear spins of 0 and 1/2. Here the total angular momentum  $F$  is the sum of the electronic angular momentum  $J = 1/2$  and the nuclear spin  $I = 1/2$ . Two examples of such molecules, which have been studied in our laboratory, are  $^{174}\text{YbF}$  and  $\text{CaF}$ . In the absence of any external fields, the two hyperfine

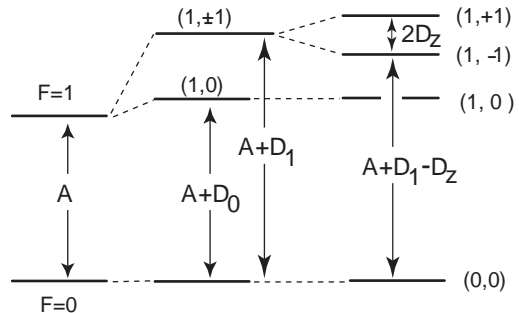


FIG. 4: Hyperfine levels. Left: field-free levels  $F = 0, 1$ . Centre: electric field induced shift of levels and tensor Stark splitting of the triplet  $F = 1$ . Right: Zeeman splitting of the doublet  $F = 1, M_F = \pm 1$ .

levels are separated by the hyperfine splitting  $A$ , as illustrated on the left of Fig. 4, and the three magnetic sublevels of  $F = 1$  are degenerate. ( $A = 2\pi \times 123$  MHz in  $\text{CaF}$  and  $2\pi \times 170$  MHz in  $\text{YbF}$ ). For a fuller discussion of hyperfine structure in such molecules, see [49]. When the molecule is subjected to an electric field  $E_z$ , the main effect is the rigid rotor Stark shift due to the electric dipole moment  $\mu_e$  along the internuclear axis of the molecule, as we discuss more fully in Sec. V. This shift is large in comparison with the hyperfine interaction; for example the  $N = 0$  state of  $\text{YbF}$  shifts downwards by 20 GHz at 20 kV/cm. To a good approximation all four hyperfine levels shift together, but there are some small differential shifts as well, due mainly to the tensor part of the hyperfine interaction between  $J$  and  $I$ , the electronic and nuclear angular momenta. This effect is analysed in detail in Ref. [49]. Relative to the  $F = 0$  level, the state  $(F, M_F) = (1, 0)$  shifts up by  $\Delta_0$  whereas states  $(1, \pm 1)$  shift up by  $\Delta_1$ , as illustrated in the centre of Fig. 4. These shifts are plotted in Fig. 5 versus electric field for the particular case of  $\text{YbF}$ . The lines are a calculation

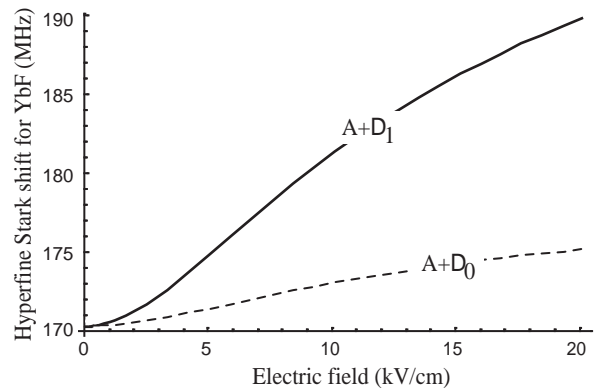


FIG. 5: Stark shift of the ground state hyperfine intervals in  $\text{YbF}$ .



following the theory detailed in [49], which has been confirmed by experiment. One sees that these shifts of the hyperfine frequencies within the  $N = 0$  manifold are typically a thousand times smaller than the over-all shift of the manifold itself. The general behaviour is a quadratic shift at low electric fields, where the characteristic dipole interaction  $-\boldsymbol{\mu}_e \cdot \mathbf{E}$  is small compared with the rotational constant  $B$ , evolving to a more nearly linear behaviour at higher fields and ultimately saturating at the highest fields.

It is worth noting that the total Hamiltonian (including the coupling to the external electric field) is invariant under time reversal. Since the two states  $\{(1, +1)$  in field  $\mathbf{E}\}$  and  $\{(1, -1)$  in field  $\mathbf{E}\}$  are time-reverses of each other and since the Hamiltonian is invariant under time reversal, it follows that the energy levels of  $(1, \pm 1)$  are exactly degenerate at all electric fields. Thus, even though the molecule has an electric dipole moment along its internuclear axis, and has an induced electric dipole moment along the applied field direction  $z$ , it does not have an electric dipole moment proportional to  $F_z$ . This is a direct consequence of time reversal symmetry. By contrast, if the electron were to have a permanent EDM  $\mathbf{d}_e$  along its spin, this would lift the degeneracy between the two levels - a direct consequence of the fact that such an EDM violates time reversal symmetry. This spin-dependent Stark shift is what our group measures in searching for an electron EDM using YbF molecules [26].

A more mundane way to split the  $(1, \pm 1)$  levels, as illustrated on the right of Fig. 4, is with a static magnetic field  $\mathbf{B}$  through the Zeeman interaction  $g_F \mu_B \mathbf{F} \cdot \mathbf{B}$ , where  $\mu_B$  is the Bohr magneton, and the  $g$ -factor expresses the ratio of magnetic moment to total angular momentum. Provided this interaction is small compared with the tensor Stark splitting  $\Delta_1 - \Delta_0$ , the molecule only responds to the component  $B_z$  parallel (or antiparallel) to the electric field. This splits the levels by  $\pm \Delta_z = \pm g_F \mu_B B_z / \hbar$ . The additional contribution to this splitting resulting from a perpendicular field component  $B_\perp$  is of order  $\Delta_z [\mu_B B_\perp / (\Delta_1 - \Delta_0)]^2$  [26] and is therefore negligible. No violation of time reversal symmetry is implied here because the state  $\{(1, -1)$  in field  $\mathbf{B}\}$  is not the time-reverse of  $\{(1, +1)$  in field  $\mathbf{B}\}$ : time reversal also reverses the sign of  $\mathbf{B}$ . There is no shift (to first order) of the states  $(F, M_F) = (0, 0)$  and  $(1, 0)$  since they have  $\langle F_z \rangle = 0$ .

To summarise, the mean shift of the two levels  $(1, \pm 1)$  relative to level  $(0, 0)$  is a measure of the electric field strength, whilst the splitting between the two measures the parallel component of magnetic field (and a possible very small contribution from the electron EDM). Although we have chosen to illustrate this with a simple hyperfine system having  $F = 0$  and  $F = 1$ , the same behaviour applies more generally, namely that any two levels  $F, \pm M_F$  are equally shifted by the Stark interaction with electric field  $E_z$ , whereas they are split apart by a magnetic field along  $z$  (and by an EDM). In the coherent manipulations we discuss below, the  $(1, 0)$  level plays no significant role and we therefore do not consider

it further. The remaining three levels can now be conveniently abbreviated to  $(0)$ ,  $(+1)$  and  $(-1)$ , with energies  $0$ ,  $A + \Delta_1 + \Delta_z$  and  $A + \Delta_1 - \Delta_z$  respectively. In the next section, we will find it convenient to redefine the zero of energy.

## B. Two-pulse interferometry of a 3-level system

Let us write the amplitudes of these three states as a column vector

$$a_z(t) = \begin{pmatrix} a_0(t) \\ a_{+1}(t) \\ a_{-1}(t) \end{pmatrix}_z, \quad (16)$$

where the subscript  $z$  indicates that the quantisation axis is taken to be along the electric field. The free evolution of these amplitudes from time  $t_1$  to time  $t_1 + \tau$  in the presence of the static electric and magnetic fields is given by the propagator

$$\Pi_0(t_1, \tau) = \begin{pmatrix} e^{i\frac{\Omega}{2}\tau} & 0 & 0 \\ 0 & e^{-i(\frac{\Omega}{2} + \Delta_z)\tau} & 0 \\ 0 & 0 & e^{-i(\frac{\Omega}{2} - \Delta_z)\tau} \end{pmatrix}_z, \quad (17)$$

such that  $a_z(t_1 + \tau) = \Pi_0(t_1, \tau) a_z(t_1)$ . Here the Stark-shifted hyperfine interval  $A + \Delta_1$  has been replaced by the symbol  $\Omega$  and we have moved the zero of energy to the centre of that interval in order to simplify the algebra that follows.

Let us suppose that the molecules are prepared in state  $(0)$ , then subjected to an rf magnetic field  $\beta_x \cos(\omega t + \phi)$  along  $x$  in order to drive transitions to states  $(+1)$  and  $(-1)$ . This field excites the coherent superposition state  $(c) = \frac{1}{\sqrt{2}}[(+1) + (-1)]$  and does not couple at all to the orthogonal superposition  $(u) = \frac{1}{\sqrt{2}}[(+1) - (-1)]$ . (The converse is true for an rf field along  $y$ ). This suggests a new basis with quantisation along the  $x$ -axis, in which the new state amplitudes are given by

$$a_x = \begin{pmatrix} a_0 \\ a_c \\ a_u \end{pmatrix}_x = U a_z \quad (18)$$

$$= \begin{pmatrix} 1 & 0 & 0 \\ 0 & \frac{1}{\sqrt{2}} & \frac{1}{\sqrt{2}} \\ 0 & \frac{1}{\sqrt{2}} & -\frac{1}{\sqrt{2}} \end{pmatrix} \begin{pmatrix} a_0 \\ a_{+1} \\ a_{-1} \end{pmatrix}_z.$$

Note that the transformation  $U$  is its own inverse:  $U = U^{-1}$ . In the  $x$ -basis, only the states  $(0)$  and  $(c)$  are coupled by the rf field. With this reduction of the problem to a two-level problem, we can write down how the amplitudes evolve in the  $x$ -basis under the influence of the rf magnetic field applied from time  $t_1$  to time  $t_1 + \tau$ .

Following the standard derivation leading to Eq. V.7 of Ramsey's book [50], we find that

$$\Pi_{\text{rf}}(t_1, \tau) = \begin{pmatrix} Ze^{i\frac{\omega}{2}\tau} & We^{i\frac{\omega}{2}\tau}e^{i(\omega t_1 + \phi)} & 0 \\ We^{-i\frac{\omega}{2}\tau}e^{-i(\omega t_1 + \phi)} & Z^*e^{-i\frac{\omega}{2}\tau} & 0 \\ 0 & 0 & e^{-i\frac{\omega}{2}\tau} \end{pmatrix}_x, \quad (19)$$

where

$$\begin{aligned} Z &= i \cos \Theta \sin\left(\frac{a\tau}{2}\right) + \cos\left(\frac{a\tau}{2}\right) \\ W &= i \sin \Theta \sin\left(\frac{a\tau}{2}\right) \\ a &= \sqrt{(\Omega - \omega)^2 + 4b^2} \\ \cos \Theta &= \frac{\Omega - \omega}{a} \\ \sin \Theta &= -\frac{2b}{a} \\ b &= \langle 0 | -\mu_x \beta_x | c \rangle. \end{aligned}$$

Although the phase of the field  $\phi$  is not important when a single pulse is applied, we keep it in this formula because it becomes relevant when we consider double pulses. As the state  $(c)$  is excited, the effect of any static magnetic field  $B_z$  will be to rotate it into the third state  $(u)$  at the Larmor frequency  $\Delta_z$ . This has been ignored in deriving Eq. (19), under the assumption that the rf excitation will be performed quickly in comparison with the Larmor precession. Taken together, Eqs. (17), (18) and (19) provide us with all the tools we need to investigate the evolution of this three-level system under any sequence of short rf pulses.

When molecules in state  $(0)$  are subjected to a single rf pulse, the probability of excitation to state  $(c)$  is given by Eq.(19) as

$$\begin{aligned} P_{1\text{ pulse}}(0 \rightarrow c) &= |W|^2 \\ &= \frac{4b^2}{(\Omega - \omega)^2 + 4b^2} \sin^2\left(\frac{\tau}{2} \sqrt{(\Omega - \omega)^2 + 4b^2}\right). \end{aligned} \quad (20)$$

This is the usual magnetic resonance lineshape for transitions in a 2-level system without damping. At resonance the population oscillates sinusoidally between the two states (this is known as Rabi oscillation). A ' $\pi$ -pulse' is an on-resonance pulse with  $2b\tau = \pi$ , which transfers all the population from state  $(0)$  to state  $(c)$ . In section IV C we will discuss how this can be used in a molecular beam to map out the fields along the beamline. An on-resonance ' $\pi/2$ -pulse' ( $2b\tau = \pi/2$ ) drives the transition only half way, creating an equal superposition of states  $(0)$  and  $(c)$  with a definite relative phase. The density matrix element describing this coherence at the end of the pulse (at time  $t_1 + \tau$ ) is  $(a_0 a_c^*)_x = \frac{1}{2}i \exp\{i[\omega(t_1 + \tau) + \phi]\}$ , the phase of which (apart from the fixed factor of  $i$ ) is just the final phase of the rf field.

In conventional Ramsey spectroscopy of a 2-level system [50], two short  $\pi/2$  pulses are applied in succession.

If the second pulse comes immediately after the first, the transition is completed and all the population is excited. If instead there is a delay time  $T$  between the two pulses, which is long compared to the pulse duration  $\tau$ , the transition probability becomes sensitive to small differences between the rf frequency and the molecular transition frequency. The internal coherence evolving at the transition frequency accumulates a phase between pulses of  $\Omega T$ , whereas the rf field evolves a phase  $\omega T$ . When the difference between these two reaches  $\pi$ , the second pulse reverses the effect of the first, returning all the population to the initial state. More generally, the probability that a molecule will end up in the excited state is

$$P_{\text{Ramsey}}(0 \rightarrow 1) = \frac{1}{2} \{1 + \cos([\Omega - \omega]T - \delta\phi)\}, \quad (21)$$

where we have allowed for the useful possibility of giving the second pulse a phase  $\phi + \delta\phi$  when the first has phase  $\phi$ . These oscillations of the population, resulting from a beat between the coherence and the driving field, are known as Ramsey fringes. They are important because a long waiting time  $T$  allows a small difference  $\Omega - \omega$  to be measured, giving rise to very precise spectroscopy.

We have generalised this idea to our system of three hyperfine levels. The result, derived from Eqs. (17), (18) and (19) is

$$\begin{aligned} P_{2 \times \text{pulse}}(0 \rightarrow 1) &= \quad (22) \\ &= 1 - \cos^2(b\tau)_1 \cos^2(b\tau)_2 - \cos^2(\Delta_z T) \sin^2(b\tau)_1 \sin^2(b\tau)_2 \\ &\quad + \frac{1}{2} \cos([\Omega - \omega]T - \delta\phi) \cos(\Delta_z T) \sin(2b\tau)_1 \sin(2b\tau)_2. \end{aligned}$$

Here we allow for the possibility that the values of  $b\tau$  for the two pulses,  $(b\tau)_1$  and  $(b\tau)_2$ , are not equal. In the 'Ramsey' case of two  $\pi/2$ -pulses, this simplifies to

$$\begin{aligned} P_{2 \times \frac{\pi}{2}\text{-pulse}}(0 \rightarrow 1) &= \quad (23) \\ &= \frac{1}{4} (3 - \cos^2(\Delta_z T) + 2 \cos([\Omega - \omega]T - \delta\phi) \cos(\Delta_z T)). \end{aligned}$$

If we set  $\Delta_z$  to zero, Eq.(23) reduces to the standard two-level Ramsey result of Eq.(21) because the third state  $(u)$  plays no role when the two levels  $(+1)$  and  $(-1)$  are degenerate. When  $\Delta_z \neq 0$  it can be useful to pick out the Ramsey interference by switching  $\delta\phi$  between 0 and  $\pi$  and taking the difference, which is  $\cos([\Omega - \omega]T) \cos(\Delta_z T)$ . As the frequency of the oscillator is swept, the amplitude of these fringes provides information about the Zeeman shift  $\Delta_z$ , while the phase of the fringe pattern reveals the precise value of the splitting  $\Omega$  with a precision controlled by the choice of  $T$ . In section IV D we give an example of how this can be used to look for small changes in a large electric field.

With three levels, it becomes possible to do interferometry using  $\pi$ -pulses as well. Taking  $2bt = \pi$ , Eq.(22) becomes

$$P_{2 \times \pi\text{-pulse}}(0 \rightarrow 1) = \sin^2(\Delta_z T). \quad (24)$$

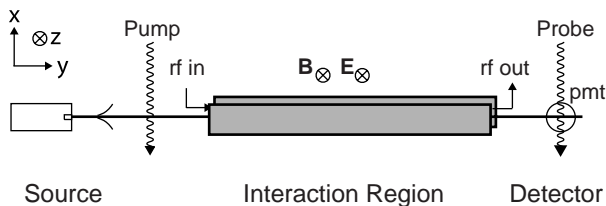


FIG. 6: Schematic diagram of the beam machine. Bunches of molecules issue from the source (in the  $y$ -direction) and are skimmed before being optically pumped into a single hyperfine state. The molecules enter the magnetically shielded interaction region and fly through a high-voltage capacitor where electric and magnetic fields can be applied along  $z$ . This doubles as an rf transmission-line where the rf magnetic field is along  $x$ . Finally, the molecules are detected by laser induced fluorescence.

This has a simple interpretation. Molecules are excited by the first pulse to state ( $c$ ). This state subsequently evolves into  $\cos(\Delta_z T)(c) + i \sin(\Delta_z T)(u)$  because of the splitting between states ( $+1$ ) and ( $-1$ ). The second pulse then drives the state- $(c)$  part of the population back to ( $0$ ), leaving those in state ( $u$ ) alone. As the magnetic field is scanned, this produces fringes in the final state- $(0)$  population, with a spacing that is inversely proportional to  $T$ . These interference fringes can be used for sensitive magnetometry and in searching for an electron EDM.

### C. Experiments with single pulses

Precision measurements usually require careful control and monitoring of stray and applied fields, both electric and magnetic, throughout the interaction region of the apparatus. The small spatial and temporal extent of molecular beam pulses make it possible to do so with high spatial resolution [51]. Fig. 6 shows an apparatus to demonstrate this using YbF molecules and pulsed rf fields. A pump laser and an interaction region have been added in between the source and detector already shown in Fig. 1. Although the beam is cold, both hyperfine levels are occupied because the splitting  $A = 170$  MHz is very much less than  $kT$ . The pump laser excites the  $A^2\Pi_{1/2} - X^2\Sigma^+$  Q(0) transition at 552 nm, for which the Doppler width is (almost) eliminated by pointing the laser beam perpendicular to the molecular beam. This makes the excitation spectrum narrow enough ( $\sim 20$  MHz) to excite just the  $F = 1$  population so that it becomes selectively depleted. The remaining  $N = 0$  molecules are virtually all in the  $F = 0$  state, which serves as the initial state for subsequent manipulation by rf pulses.

The interaction region starts 450 mm from the skimmer and is 790 mm long. It is magnetically shielded to reduce the ambient field, whilst current-carrying wires inside the shields can generate a magnetic field if required. Within this region there is a pair of electric field

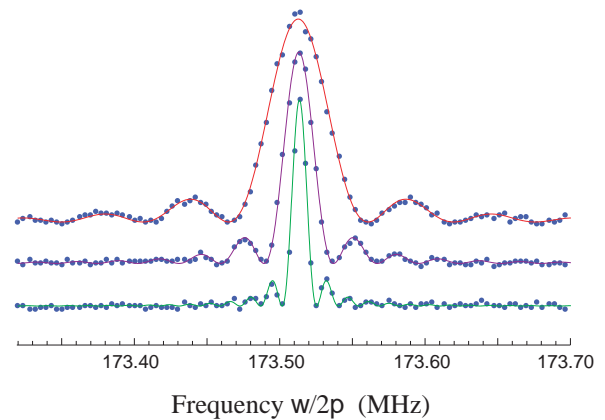


FIG. 7: Excitation spectra for the ground state  $F = 0 \rightarrow F = 1$  transition in YbF using  $\pi$ -pulses of three different pulse lengths (upper,  $\tau = 18 \mu\text{s}$ ; middle,  $\tau = 36 \mu\text{s}$ ; lower,  $\tau = 72 \mu\text{s}$ ). A static electric field of 12.5 kV/cm is applied. Dots: experimental data. Lines: plots of Eq. 20.

plates, 750 mm long and 70 mm wide, with a 12 mm spacing, constant to better than 200  $\mu\text{m}$  over the full length. These are machined from cast aluminium, then gold coated to improve the uniformity of the surface potential (using a non-magnetic, nickel-free process). The whole assembly is non-magnetic. With a field across the gap of 15 kV/cm the leakage current is less than 1 nA.

The same plate structure also serves as a 34  $\Omega$  transmission line for the rf field, transporting it as a 170 MHz TEM wave travelling parallel or antiparallel to the beam direction. This is described more fully in [51]. As a bunch of molecules travels along the interaction region, a hyperfine transition can be induced at any desired position by pulsing the rf field on for a short time. This repopulates the  $F = 1$  state and therefore produces an increase in the fluorescence signal at the detector, as shown by the rf frequency scans in Fig. 7. Being a TEM wave, the rf magnetic field between the plates is accurately perpendicular to the static electric field and we choose to define its direction as the  $x$ -axis. This field therefore drives the transition ( $0$ ) – ( $c$ ) discussed in the last section.

Fig. 7 shows three excitation spectra, obtained by applying  $\pi$ -pulses of three different durations (18, 36, and 72  $\mu\text{s}$ ) to molecules near the middle of the interaction region. Superimposed on the data points are solid lines corresponding to Eq. (20), which does a good job of describing the lineshapes, including the positions and relative heights of the sidebands. When we fix the value of  $2b\tau$  at some value  $\theta$  (equal to  $\pi$  in this case), these lineshapes can be re-written as a universal function  $\sin^2(\frac{\theta}{2}\sqrt{1+x^2})/(1+x^2)$ , where  $x = (\Omega - \omega)\tau/\theta$ . Thus, the width of the line is inversely related to the duration of the pulse, becoming wider as the pulse is made shorter, as one would expect from the usual Fourier relation between pulse duration and spectral width. For a  $\pi$ -pulse, the full width at half maximum is  $\delta\omega_{\text{FWHM}} = 5.0/\tau$ .

The transition probabilities in Fig. 7 peak at

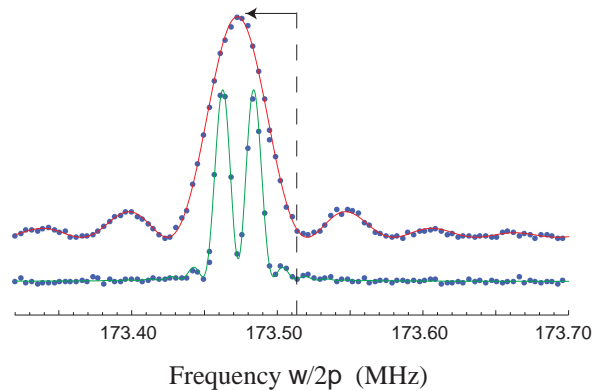


FIG. 8: Upper curve: the hyperfine transition moves to lower frequency when the electric field is reduced. The dashed line marks the line-centre of Fig. 7 at higher electric field. Lower curve: The line splits when a magnetic field is applied.

173.513 MHz, not at the field-free frequency of 170.254 MHz, because these spectra were measured with a potential difference of 15 kV across the 12 mm gap of the plates and are therefore Stark-shifted by  $\Delta_1$ , as illustrated in Fig. 4. The magnitude of this shift is a measure of the electric field strength at the place occupied by the molecules when the rf pulse was applied. By varying the timing of the rf pulse, it is possible to map out the electric field as a function of position along the beamline [51]. Note that the Doppler shift of the rf transition is only a few hundred Hz and is therefore insignificant at this level of accuracy. In Fig. 8 we show how the resonance frequency moves down (by 40.246 kHz) when the applied potential difference is reduced (by 203 V). The spectral resolution afforded by the  $18 \mu\text{s}$   $\pi$ -pulses is quite sufficient to see this shift clearly. Fig. 8 also shows how the line splits by  $2\Delta_z$  (see Fig. 4) when a DC magnetic field of  $0.8 \mu\text{T}$  is applied. In order to resolve the 22 kHz splitting fully, the linewidth was narrowed by increasing the pulse duration to  $72 \mu\text{s}$ . Over this time, a YbF molecule travelling at 590 m/s covers 42 mm, so it has been necessary to give up some spatial resolution in order to achieve the higher spectral resolution. The use of long rf pulses for high precision spectroscopy is not ideal because the static field average that is measured can be affected in a complicated way by variations in the strength and polarisation of the rf field, either in space or in time. As was first pointed out by Ramsey, it can be more satisfactory to use a pair of rf pulses, and that is what we discuss next.

#### D. Experiments with double pulses

In Eq. (23), we found an expression for the lineshape using two short  $\pi/2$ -pulses separated by a time  $T$ . In order to pick out the Ramsey interference, we suggested introducing a phase shift  $\phi$  between the first and sec-

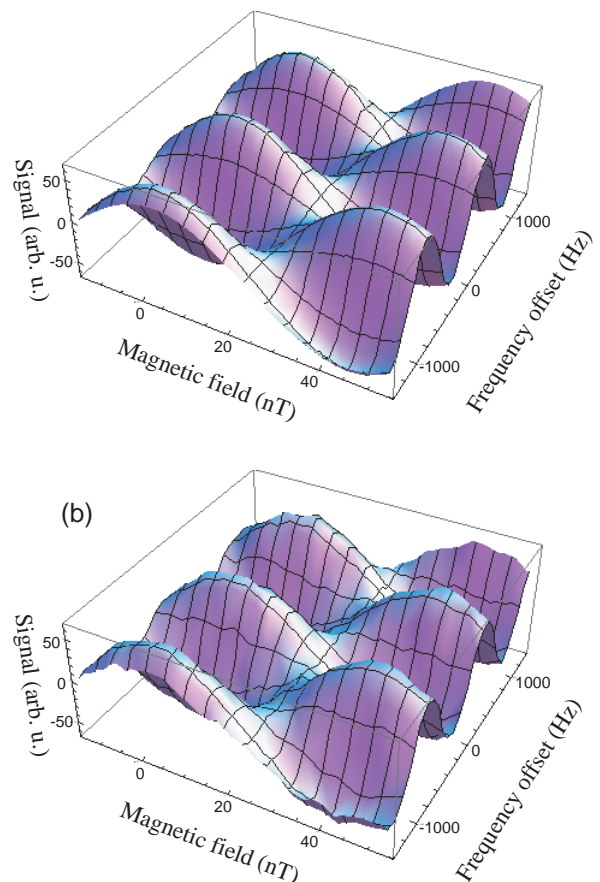


FIG. 9: Ramsey interference signals using two  $\pi/2$ -pulses separated by a time  $T = 900 \mu\text{s}$ . The signals are plotted versus the rf frequency  $\omega$  and also as a function of magnetic field in nT. (a) Theoretical signal, scaled to have the same amplitude as the experimental result. (b) Measured Ramsey interference, in excellent agreement with the theory.

ond pulse and taking the difference between  $\phi = \pi$  and  $\phi = 0$ . This is expected to give fringes of the form  $\cos(\Delta_z T) \cos([\Omega - \omega]T)$ , which we have plotted in Fig. 9(a) versus rf frequency and magnetic field for the case when  $T = 900 \mu\text{s}$ . In Fig. 9(b) we display the result of an experiment to test this formula, in which we scanned the rf frequency  $\omega$  many times through a region close to  $\omega = \Omega$ , stepping the applied magnetic field  $B_z$  in order to vary the Zeeman splitting  $2\Delta_z$ . In this experiment, the molecules perform exactly as predicted by Eq. (23).

In Fig. 10, we scan a much wider frequency range, covering the central 40 Ramsey fringes with  $B_z$  fixed close to zero. Here we begin to see a departure from Eq. (23) in the amplitude of the fringe pattern, which shows a clear decrease on either side of the centre. This happens because the individual pulses are starting to become appreciably detuned, and therefore have reduced amplitude. Indeed, when the detuning reaches  $\pm\sqrt{15}/(4\tau) = \pm 54 \text{ kHz}$ , the  $18 \mu\text{s}$  single pulse transition probabilities go

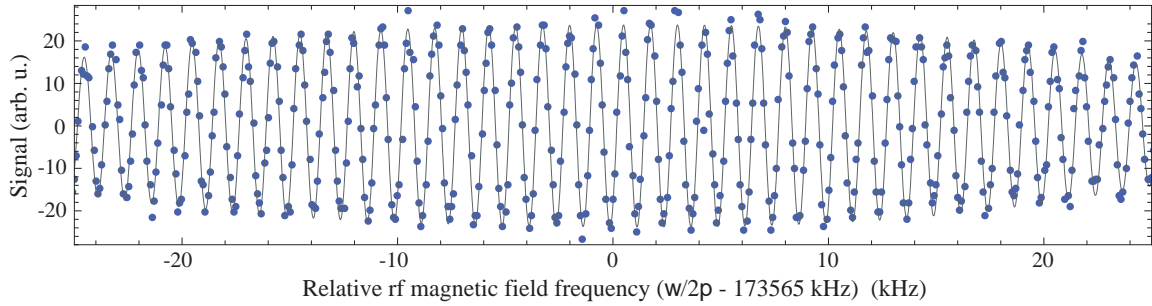


FIG. 10: The central 40 fringes of a Ramsey pattern obtained using two  $\pi/2$ -pulses of  $18\mu\text{s}$  duration, separated by  $T = 800\mu\text{s}$ . The magnetic field is set very close to zero. Dots: Experimental points. Line: Theoretical fringes with amplitude adjusted to fit the data.

to zero and the Ramsey interference has no amplitude at all. For a 2-level system, the envelope of the interference pattern is just the single-pulse lineshape, as discussed by Ramsey [50]. However, the spectrum of Fig. 10 involves the third level ( $u$ ), which makes it sensitive to very small magnetic fields and complicates the shape of the envelope. This detuning effect is not included in Eq. (22), which assumes that the detuning is small compared with  $1/\tau$ . At present we do not have an analytical formula for this case, so the varying amplitude of the  $-\cos([\Omega - \omega]T)$  curve drawn through our data in Fig. 10 is just a smooth fit to the measured amplitude of the oscillations.

The curve in Fig. 11 shows a blow-up of the central Ramsey fringe (solid line), together with the fringe obtained when the high voltage leads were reversed (dashed line). The small shift in the phase of the fringe pattern shows that the  $12.5\text{ kV/cm}$  electric field decreased in magnitude by  $455 \pm 11\text{ mV/cm}$  when we attempted to reverse it. This experiment demonstrates that Ramsey interferometry of the hyperfine states can provide very sensitive monitoring of high electric fields in a molecular

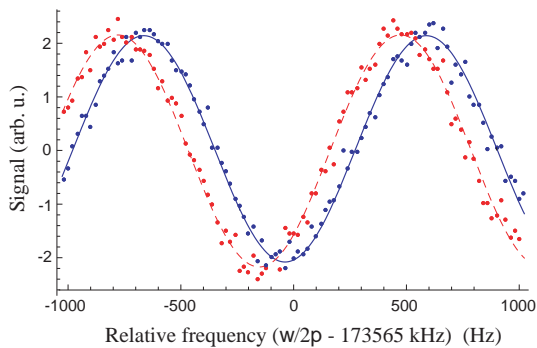


FIG. 11: The central fringe of Fig. 10. Solid line: fit to data taken with electric field as in Fig. 10. Dashed line: fit to data taken with high voltage leads reversed. The evident Stark shift between the two indicates a change in the magnitude of the electric field

beam apparatus.

We turn now to interferometry using pairs of  $\pi$ -pulses. Whereas the  $\pi/2$ -pulses of Ramsey interferometry prepare and interrogate an rf coherence between the states (0) and (c), the  $\pi$  pulses make and probe the superposition of the states (+1) and (-1), which are almost degenerate. As expressed in Eq. (24), this superposition evolves at the ( $\pm 1$ ) splitting frequency, leading to fringes of the form  $\sin^2(\Delta_z T)$ , where  $\hbar\Delta_z = g_F \mu_B B_z$ . Figure 12 shows the interferometer fringes measured in an electric field of  $10\text{ kV/cm}$  by scanning the applied magnetic field over  $160\text{ nT}$ , with a separation of  $T = 800\mu\text{s}$  between the two  $\pi$ -pulses. The solid line is a fit over the two central fringes to the lineshape  $A \sin^2(\Delta_z T) + C$ , where  $C$  represents the background due to unpumped  $F = 1$  molecules and to scattered light. Within the 2% uncertainty of the applied magnetic field calibration, the fringe spacing is found to be  $44\text{ nT}$ , corresponding to a  $g_F = 1$ , as one would expect for the  $F = 1$  hyperfine level of this  $^2\Sigma$  state. The total field  $B_z$ , which determines  $\Delta_z$ , is taken in our fit to have an adjustable offset in addition to the applied field. This is found to be  $1.7\text{ nT}$  in Fig. 12, which is typical of the field that leaks through the magnetic shielding from outside. While this simple function

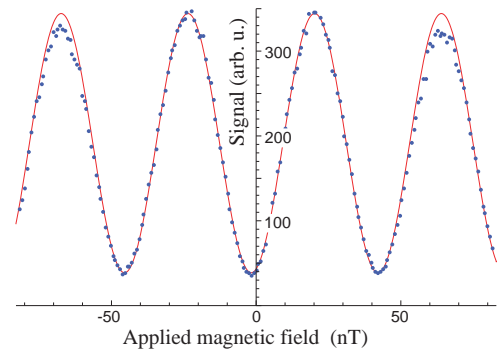


FIG. 12: Interferometer fringes obtained by scanning the applied magnetic field, using a pair of  $\pi$ -pulses, separated in time by  $800\mu\text{s}$ . Dots: experimental data. Line: a fit of the central two fringes to the form  $A \sin^2(\Delta_z T) + C$ .

fits the central two fringes well, the next fringe on either side clearly has less amplitude. This is because the magnetic field detunes the two  $\pi$ -pulse transitions from resonance.

Adjusting the magnetic field to reach a steep part of the fringe pattern, the interferometer becomes sensitive to any small change in the splitting  $2\Delta_z$  between the levels ( $\pm 1$ ). This can be used to monitor variations of the magnetic field in the apparatus. In addition, if the electron has a dipole moment  $d_e$ , then the interaction with the applied electric field  $E$  also contributes to  $\Delta_z$ , the additional amount being  $\pm d_e \eta E / \hbar$ . Here  $\eta$  is the enhancement factor discussed in Sec.II B. If the electric field is reversed, this shift changes sign, causing the fringe pattern to be modulated from side to side as the electric field is flipped back and forth. In this way, a measurement of the signal on the side of a fringe can become very sensitive to the presence of a small electron EDM.

## V. ALTERNATING GRADIENT DECELERATION OF POLAR MOLECULES

### A. Introduction

We have seen in section IV how spectral resolution can be improved by increasing the time  $T$  available for coherent evolution. In a molecular beam with a velocity of a few hundred m/s and an interaction region 1 m long, this time is a few ms, corresponding to minimum linewidths of several hundred Hz. For this reason, the prospect of decelerating and trapping molecules offers significant improvements for some precision measurements, provided the beam flux can remain high and the inhomogeneous broadening due to trapping fields can be kept under control. The basic idea of deceleration is to manipulate polar molecules in an electric field gradient using the force due to the Stark effect. After Stark deceleration was first demonstrated [52], the new technology was rapidly applied to make new measurements. Using a beam of  $^{15}\text{ND}_3$  molecules decelerated to 52 m/s, the energies of all 22 hyperfine levels of the  $(J,K)=(1,1)$  state were measured with accuracies better than 100 Hz [14]. Using Stark-decelerated OH radicals, greatly improved measurements of the ground-state  $\Lambda$ -doublet microwave transitions were made, thus contributing to the constraint on the evolution of the fine-structure constant over cosmological time [8]. Once molecules could be trapped, it became possible to measure directly the lifetimes of long-lived molecular states [53], and even to measure the optical pumping of molecules by room temperature blackbody radiation [54], which typically occurs on a timescale of many seconds.

Many of the precision measurements discussed in this chapter make use of heavy polar molecules. Stark deceleration of these heavy species is considerably more challenging because (i) the kinetic energy to be removed is proportional to the molecular mass and (ii) the low-lying energy states are all high-field-seeking whereas the Stark

deceleration method works best for low-field seekers. The first difficulty arises because the molecules formed in a supersonic expansion acquire the speed of the carrier gas into which they are seeded; thus their speed is independent of their mass. This difficulty could be mitigated by using a low-temperature effusive source such as the buffer-gas sources recently demonstrated [55, 56].

The second difficulty results from the closely packed rotational energy levels of a heavy molecule which causes all the low-lying states to be high-field seeking when the electric field is strong. This problem is best illustrated by considering the Stark shift of a rigid rotating molecule of reduced mass  $m'$ , bond-length  $R$  and dipole-moment  $\mu$ . The Hamiltonian is  $H = B\vec{J}^2 - \vec{\mu} \cdot \vec{E}$ , where  $B = \hbar^2 / (2m'R^2)$  is the rotational constant,  $\vec{J}$  is the angular momentum vector and  $\vec{E}$  is the applied electric field. Figure 13 shows the first 16 energy eigenvalues, in units of  $B$ , as a function of applied electric field, in units of  $B/\mu$ . The field mixes states having different values of  $J$  but the same value of  $M$ , the projection of the angular momentum onto the electric field axis. Each energy level is labelled according to the quantum numbers  $(J, M)$  that the state evolves into when the electric field is adiabatically reduced to zero. Note that the states  $(J, M)$  and  $(J, -M)$  are degenerate for all electric fields, a consequence of time-reversal-symmetry. The important point to note from Fig. 13 is that all the weak-field seeking states have turning points, becoming strong-field-seekers at high field. For example, the lowest-lying weak-field seeking state  $(1, 0)$  has its turning point at an electric field of  $4.9B/\mu$ , at which point the Stark shift is  $0.64B$ . Taking YbF as an example of a molecule with a small rotational constant, the electric field at the turning point is only 18 kV/cm and the Stark shift only  $0.15 \text{ cm}^{-1}$ . This amount of energy, which can be removed from the molecule in a single stage of deceleration, is to be compared with the  $682 \text{ cm}^{-1}$  of kinetic energy possessed by a YbF molecule formed in a supersonic expansion at 290 m/s [46]. Clearly a very large number of stages would be needed to decelerate in this way. By contrast, the strong-field-seeking ground-state of YbF has a Stark shift of  $10.7 \text{ cm}^{-1}$  at a field of 200 kV/cm, and so Stark deceleration in this state seems feasible. For more complex molecules, such as those of biological interest, the situation is even more extremely weighted in favour of the high-field-seekers, as discussed in more detail in [57].

Unlike weak-field-seekers, which are naturally focussed onto the axis of the Stark decelerator, strong-field-seeking molecules cannot be focussed using static fields. A dynamic focussing scheme needs to be employed to prevent the molecules being pulled towards the surfaces of the electrodes, where the field is strongest. The alternating gradient focussing technique solves this problem of transverse confinement. The molecules travel through a sequence of electrostatic lenses, each of which focusses the molecules in one of the two transverse directions and defocusses them in the other. The focussing and defocussing planes alternate between one lens and the next.

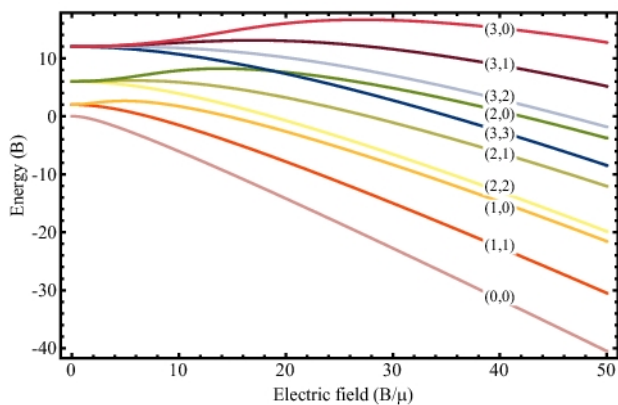


FIG. 13: The Stark shift of the low-lying energy levels of a rigid rotating molecule. The electric field is expressed in units of  $B/\mu$  and the energy in units of  $B$ . States are labelled by the quantum numbers  $(J, M)$ .

For a subset of the molecules that enter the decelerator, namely those that lie within the transverse phase-space acceptance of the lens array, the net effect is to focus in both transverse planes. Ideally, the focussing and defocussing forces are linear in the off-axis displacements, and the trajectories of the accepted molecules take them far from the axis inside the focussing lenses, but close to the axis inside the defocussing lenses. Thus, the overall focussing is a direct result of the motion of the molecules, and can operate even when the defocussing power is stronger than the focussing.

The first experiment to demonstrate alternating gradient deceleration of polar molecules used an array of 12 lenses to decelerate high-field-seeking metastable CO molecules from 275 to 260 m/s [58]. Ground-state YbF molecules were decelerated from 287 to 277 m/s using a similar machine [59]. The transverse focussing properties of the alternating gradient have been demonstrated [57] by imaging metastable CO molecules exiting from the decelerator. Longer machines, with more sophisticated electrode designs, should be capable of decelerating heavy polar molecules to rest.

### B. A model alternating gradient decelerator

We consider a decelerator consisting of a series of electrostatic lenses whose focussing and defocussing planes alternate. A typical electrode structure is shown in Fig. 14(a). Here, each lens is formed by applying a large potential difference between a pair of rods whose axes lie parallel to the beamline. The forward velocity of the molecules only changes when they pass through the fringe fields formed in the gap that separates one lens from the next. In operation, the decelerator is switched between three states: (i) odd lenses at high voltage, even lenses grounded, (ii) even lenses at high voltage, odd lenses grounded and (iii) all lenses grounded. We would like to

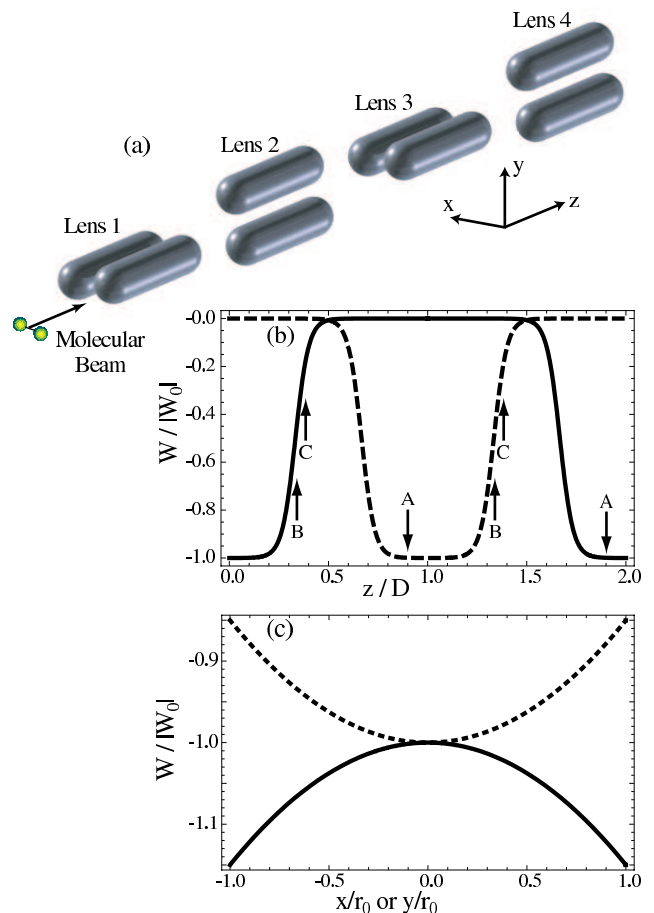


FIG. 14: (a) Schematic of a typical electrode structure in an alternating gradient decelerator. (b) Potential in which the molecules move, approximated using an analytical form (see text). Solid and dashed lines represent respectively the switch states (i) and (ii) of the decelerator. Positions A, B and C are referred to in the text. (c) At the centre of the first lens, the potential along  $x$  is shown by the solid line and that along  $y$  by the dashed line.

work out the dynamics of molecules in such a decelerator. We therefore first generate a map of the electric field in the decelerator using an electrostatics solver, and then construct the interaction potential, using the electric field dependence of the Stark shift such as is plotted in Fig. 13. We emphasise that this is not the electrostatic potential, but rather the Stark potential in which the molecules move. The electrode geometry shown in Fig. 14(a) is one of many possible geometries, some of which have been discussed in detail in reference [57]. The same reference discusses the Stark shift and shows that it varies linearly with the electric field magnitude for most heavy molecules in the electric fields of a typical decelerator. The potential in which the molecules move is similar in form for all the electrode geometries and molecular states considered, though they vary in their details. Here, we do not specialize to a particular geometry or molecular state, but instead elucidate the dynamics using an ana-

lytical form for the potential that approximates the true potential produced in most cases.

We take the potential in switch state (i) to be

$$W(x, y, z) = W_0(1 + \beta((x/r_0)^2 - (y/r_0)^2))f(z), \quad (25)$$

where

$$f(z) = \frac{\tanh(z'/d + L/2d) - \tanh(z'/d - L/2d)}{2 \tanh(L/2d)} \quad (26)$$

provides a good phenomenological approximation to the actual  $z$ -dependence. In Eq. (25),  $W_0$  is the electric field at the origin,  $r_0$  is a measure of the transverse aperture of the decelerator, and  $\beta$  measures the transverse curvature of the potential. In Eq. (26),  $z' = \text{mod}(z - D, 2D) - D$ , where  $\text{mod}(m, n)$  is the remainder on division of  $m$  by  $n$ ,  $D$  is the lens-to-lens spacing,  $L$  measures the length of a lens, and  $d$  measures how rapidly the potential changes at the exit of the lens. The potential in switch state (ii) is simply  $W(y, x, z - D)$ .

Figure 14(b,c) shows the potential for the case where  $L = 2/3D$ ,  $d = 1/15D$  and  $\beta = 0.15$ . We shall use these parameters throughout. Part (b) is a plot of the potential along the beamline,  $W(0, 0, z)$ , for both switch state (i) (solid line) and switch state (ii) (dashed line). Part (c) of the figure shows the transverse potentials in the centre of a lens,  $W(x, 0, 0)$  (solid line) and  $W(0, y, 0)$  (dotted line). In our ideal lens, these are everywhere equal and opposite.

### C. Axial motion

Consider molecules travelling down the axis of the decelerator. To calculate when we should switch the potentials we introduce the concept of a synchronous molecule, which enters the decelerator with speed  $u_0$ . We design the switching sequence so that this molecule is always at the same relative position in the periodic array every time the field is turned on (e.g. position A in Fig. 14(b)) and every time the field is turned off (e.g. position B in Fig. 14(b)). We refer to these fixed positions as  $z_{\text{on}}$  and  $z_{\text{off}}$ . Since this molecule is always climbing potential hills, it decelerates as it moves along the beamline, and the time intervals between successive switches must be chosen to increase in correspondence. The required time sequence can be constructed using a simple algorithm. Consider the energy conservation equation that applies between the turn-on and turn-off points,  $z_{\text{on}}$  and  $z_{\text{off}}$ ,

$$\frac{1}{2}Mu_{n-1}^2 + W(z_{\text{on}}) = \frac{1}{2}M(dz/dt)^2 + W(z). \quad (27)$$

Here,  $z$  is the position of the molecule at time  $t$ . Rearranging and then integrating gives us the relationship

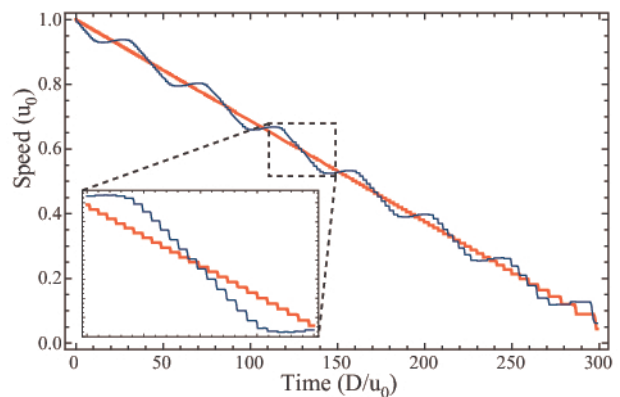


FIG. 15: The speed of a synchronous (thick red line) and a non-synchronous molecule (thin blue line) as a function of time, using the model potential and the turn-on and turn-off points A and B indicated in Fig. 14(b). The inset reveals the step-like structure of the deceleration.

between the  $n^{\text{th}}$  turn-off time,  $t_{\text{off},n}$ , and the  $n^{\text{th}}$  turn-on time,  $t_{\text{on},n}$

$$t_{\text{off},n} = t_{\text{on},n} + \int_{z_{\text{on}}}^{z_{\text{off}}} \frac{dz}{\sqrt{u_{n-1}^2 + 2(W(z_{\text{on}}) - W(z))/M}}, \quad (28a)$$

where  $u_n$  is the speed of the synchronous molecule immediately after the  $n^{\text{th}}$  turn-off. The  $(n+1)^{\text{th}}$  turn-on is now found using

$$u_n = \sqrt{u_{n-1}^2 + 2(W(z_{\text{on}}) - W(z_{\text{off}}))/M}, \quad (28b)$$

$$t_{\text{on},n+1} = t_{\text{off},n} + \frac{D - (z_{\text{off}} - z_{\text{on}})}{u_n}. \quad (28c)$$

Since we now have the potential seen by the molecules as a function of both position and time, we can solve the equation of motion numerically for any molecule, synchronous or not. Let us define  $N$  to be the minimum number of stages required to stop the synchronous molecule of mass  $M$  and initial speed  $u_0$ , through the relation  $|W_0| = Mu_0^2/(2N)$ . Figure 15 shows the result of such a calculation for the case where  $L = 2/3D$ ,  $d = 1/15D$  and  $N = 80$ , and the turn-on and turn-off points are ‘A’ and ‘B’ in Fig. 14(b). The thick red line shows the speed of the synchronous molecule versus time, while the thin blue line shows how the speed changes with time for a molecule that has the same initial speed as the synchronous molecule but starts out ahead by  $D/15$ . The deceleration of the synchronous molecule appears to be uniform, though when magnified, as in the inset, is actually seen to be a series of small steps reflecting the shape of the potential. These steps can also be seen in the main figure when the speed is low. The speed of the non-synchronous molecule oscillates around that



of the synchronous one and also consists of many small steps when examined in detail. If we take snapshots of the position and velocity of the molecules at each of the many turn-off times, we would no longer be able to see the fine structure of the motion. Between one snapshot and the next, the change in kinetic energy of the synchronous molecule is  $\Delta K = Mu\Delta u = MDu\Delta u/\Delta z_s = W(z_{\text{on}}) - W(z_{\text{off}})$ , where we have introduced the quantity  $\Delta z_s$  to represent the change in position of the synchronous molecule between one snapshot and the next, and have used the fact that  $\Delta z_s = D$  always. Since we have discarded the information about the fine structure of the motion, the deceleration of the synchronous molecule appears to be constant, and we can convert to continuous variables. The above equation then becomes  $MDu du/dz_s = MD d^2 z_s/dt^2 = W(z_{\text{on}}) - W(z_{\text{off}})$ . Applying a similar reasoning to any other molecule, described by the position and velocity coordinates  $z$  and  $v$ , we obtain  $MD d^2 z/dt^2 = W(z_{\text{on}} + \tilde{z}) - W(z_{\text{off}} + \tilde{z})$ , where  $\tilde{z} = z - z_s$ , and we have made the additional approximation that  $v - u \ll u$  so that the distance moved by the general molecule between switching times is also very close to  $D$ . Subtracting the equation for the general molecule from that for the synchronous molecule we obtain an equation of motion for the relative coordinate, allowing us to define an effective force,  $F_{\text{eff}}$ :

$$\begin{aligned} \frac{d^2 \tilde{z}}{dt^2} &= \frac{W(z_{\text{on}} + \tilde{z}) - W(z_{\text{on}}) - W(z_{\text{off}} + \tilde{z}) + W(z_{\text{off}})}{MD} \\ &= F_{\text{eff}}/M. \end{aligned} \quad (29)$$

Introducing the relative velocity  $\tilde{v} = v - u = d\tilde{z}/dt$ , the left hand side of the above equation can be written as  $\tilde{v} d\tilde{v}/d\tilde{z}$ . Integrating, we then obtain

$$1/2M\tilde{v}^2 + (V(\tilde{z}) - V(0)) = E_0, \quad (30)$$

where  $E_0$  is a constant and

$$V(\tilde{z}) = - \int F_{\text{eff}} d\tilde{z} \quad (31)$$

is an effective potential for the relative motion between non-synchronous and synchronous molecules.

Figure 16(a) shows the effective potential obtained from Eqs. (25), (26) and (31). The solid line corresponds to  $z_{\text{on}} = -D/10, z_{\text{off}} = D/3$ , while the dashed line has  $z_{\text{off}} = 11D/30$  corresponding to greater deceleration, but a shallower effective potential. Since the effective potential is confining, non-synchronous molecules with insufficient energy to reach the top of the potential must oscillate about the synchronous molecule. We can use the effective force to solve for the relative motion of non-synchronous molecules. Parts (b) and (c) of Fig. 16 show trajectories in phase-space obtained in this way, for the solid and dashed effective potentials shown in part (a). In each case, the thicker line separates bounded

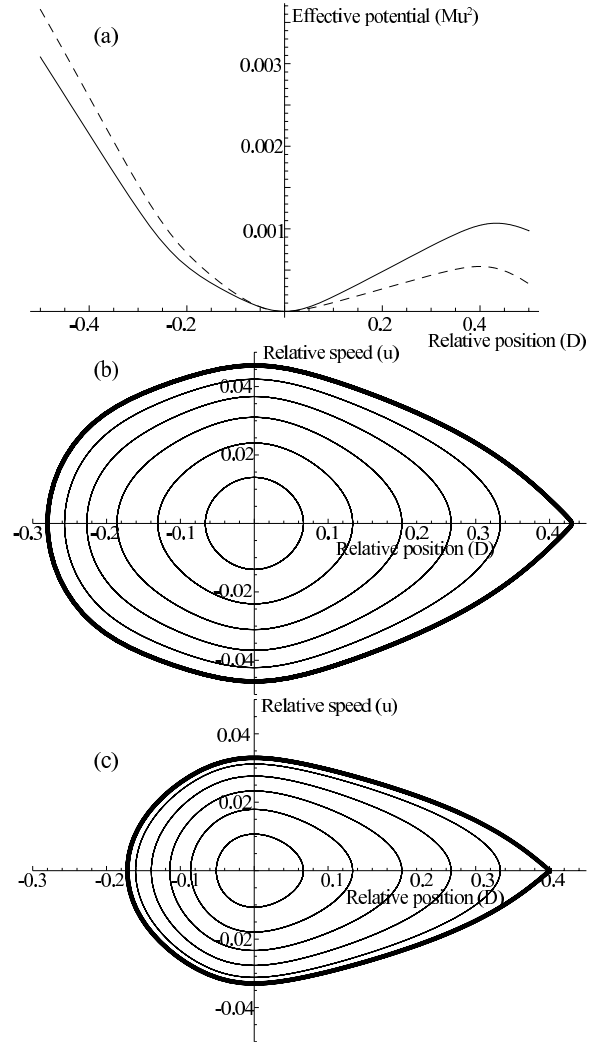


FIG. 16: (a) The effective potential, Eq. (31), as a function of relative position. The solid line corresponds to moderate deceleration (turn off position ‘B’), while the shallower potential shown by the dashed line is for strong deceleration (turn off position ‘C’). The trajectories in phase-space calculated using these effective potentials are shown in (b) and (c) for the deep and shallow potentials respectively. The thick outer boundaries in these plots are the separatrices.

and unbounded motion and is called the separatrix. All molecules inside the separatrix will remain close to the synchronous molecule throughout the deceleration process, and the area bounded by the separatrix is the axial phase-space acceptance. Comparing parts (b) and (c) of the figure, we see that, as expected from the shallower potential, the acceptance is smaller when the deceleration is greater. We note that the same phase-space plots can be generated without making use of the effective potential, by numerically integrating the complete equation of motion as was done in generating Fig. 15. The trajectories in phase space then acquire the detailed structure shown in the inset of that figure, but are otherwise found

to be identical to those obtained (much more rapidly) from the effective potential.

For small-amplitude oscillations about the synchronous molecule, the motion is harmonic. Expanding the right hand side of Eq. (29) in a Taylor series about  $\tilde{z} = 0$ , gives  $d^2\tilde{z}/dt^2 - (W'(z_{\text{on}}) - W'(z_{\text{off}}))\tilde{z}/(MD) = 0$  where  $W'(a) = dW/dz$  evaluated at  $z = a$ . The angular oscillation frequency for small-amplitude axial oscillations is therefore

$$\omega_z = \sqrt{\frac{W'(z_{\text{off}}) - W'(z_{\text{on}})}{MD}}. \quad (32)$$

For our model potential, the solid line in Fig. 16(a), the frequency can be conveniently expressed as  $\omega_z/2\pi = 0.309 u_0/(\sqrt{ND})$ . For example, if  $D = 30$  mm, and  $N = 80$  when  $u_0 = 300$  m/s, we find  $\omega_z/2\pi = 345$  Hz for turn-off at position 'B'.

#### D. Transverse motion

Our model potential is harmonic in the two transverse directions, with a curvature that varies with  $z$ . As a molecule travels through a lens, the curvature is very nearly constant until it reaches the fringe-field of the lens where the curvature drops rapidly to zero. To simplify the analysis, we make the approximation that the curvature has the constant value,  $W_0\beta/r_0^2$  over the lens length  $L$ , is zero in the drift space of length  $S = D - L$ , and changes abruptly between these values. As the decelerator structure is periodic in  $z$ , it is natural to write the equation of motion with independent variable  $z$  rather than time. For a molecule with forward speed  $u$ , the equation of motion is

$$d^2x/dz^2 + \kappa^2 Q(z)x = 0, \quad (33)$$

where  $Q(z) = 1$  inside a focussing lens,  $-1$  in a defocussing lens and  $0$  in a drift region, and the spatial frequency is

$$\kappa = \sqrt{\frac{2W_0\beta}{Mu^2r_0^2}} = \sqrt{\frac{\beta}{Nr_0^2}}. \quad (34)$$

The angular frequency of the transverse oscillation inside a focussing lens is independent of the beam velocity  $u$  and is related to  $\kappa$  by  $\Omega = \kappa u$ .

In moving through a region of length  $l$ , from an initial axial position  $z_0$ , the transverse position and velocity coordinates of a molecule change according to

$$\begin{pmatrix} x/r_0 \\ v_x/\Omega r_0 \end{pmatrix}_{z_0+l} = M(z_0+l|z_0) \begin{pmatrix} x/r_0 \\ v_x/\Omega r_0 \end{pmatrix}_{z_0}. \quad (35)$$

Here, the dimensionless transfer matrix denoted by  $M(z_0+l|z_0)$  takes the values  $F(l)$  inside a focussing lens,

$D(l)$  inside a defocussing lens and  $O(l)$  in a drift region, with

$$F(l) = \begin{pmatrix} \cos(\kappa l) & \sin(\kappa l) \\ -\sin(\kappa l) & \cos(\kappa l) \end{pmatrix}, \quad (36a)$$

$$D(l) = \begin{pmatrix} \cosh(\kappa l) & \sinh(\kappa l) \\ \sinh(\kappa l) & \cosh(\kappa l) \end{pmatrix}, \quad (36b)$$

$$O(l) = \begin{pmatrix} 1 & \kappa l \\ 0 & 1 \end{pmatrix}. \quad (36c)$$

If, in moving from left to right, the molecule first travels through a region described by the matrix  $M_1$ , followed by a region described by  $M_2$ , the matrix in Eq. (35) is simply the product,  $M = M_2 \cdot M_1$ . In this way, one complete unit of our alternating gradient array is described by  $M = F(L) \cdot O(S) \cdot D(L) \cdot O(S)$ , and a sequence of  $N$  such units is described (in a more compact but obvious notation) by  $(FODO)^N$ . It can be shown that the molecular trajectories are stable if the well known condition  $-2 < \text{Tr}(FODO) < 2$  is satisfied (e.g. [60]).

We would like to know whether a molecule that enters the array reaches the exit. For a long decelerator, the above stability condition is a necessary but not sufficient one, since a molecule can be on a stable trajectory that takes it so far from the axis that it crashes into one of the electrodes. Rather than constructing trajectories piecewise using Eqs. (36), we follow the approach first used by Courant and Snyder in the context of the alternating gradient synchrotron [61]. We look for a solution to Eq. (33) of the general form

$$\begin{aligned} x(z) &= \sqrt{\epsilon_i \beta(z)} \cos(\psi(z) + \delta_i) \\ &= A_1 \sqrt{\beta(z)} \cos \psi(z) + A_2 \sqrt{\beta(z)} \sin \psi(z) \end{aligned} \quad (37)$$

where  $\beta$  is a  $z$ -dependent amplitude function that has the same periodicity as the AG array,  $\psi$  is a  $z$ -dependent phase, and  $\epsilon_i$ ,  $\delta_i$ ,  $A_1$  and  $A_2$  are defined by the initial conditions. By substitution into Eq. (33) we find that Eq. (37) is a valid solution provided

$$\psi(z) = \kappa \int_0^z \frac{1}{\beta(z')} dz' \quad (38)$$

and

$$-\frac{1}{4}\beta'^2 + \frac{1}{2}\beta\beta'' + \kappa^2 Q(z)\beta^2 = \kappa^2. \quad (39)$$

To find  $\beta$ , we need to make the connection to the piecewise solution already given in Eqs. (36). From Eq. (37) we have

$$x'(z) = \frac{A_1 \kappa}{\sqrt{\beta}} (-\alpha \cos \psi - \sin \psi) + \frac{A_2 \kappa}{\sqrt{\beta}} (-\alpha \sin \psi + \cos \psi) \quad (40)$$

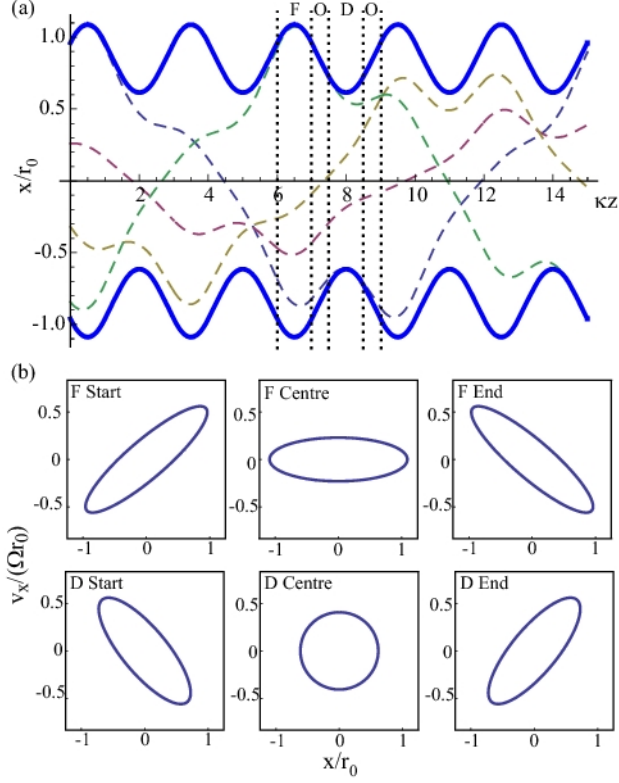


FIG. 17: (a) Dashed lines are typical trajectories through a section of the alternating gradient array. Solid lines denote the envelope that bounds the trajectories of all transmitted molecules. The positions in the array of the focussing (F), defocussing (D), and drift regions (O) are indicated by the dotted lines. The figure shows that the beam envelope is largest at the centre of the focussing lens, and smallest at the centre of the defocussing lens. (b) Evolution of the phase-space ellipse through a unit of the array.

where

$$\alpha = -\frac{1}{2\kappa}\beta'. \quad (41)$$

Using Eqs. (37) and (40) we find the relationship between the coordinates  $x, v_x/\Omega$  at position  $z$  and those at position  $z + l_{\text{cell}}$ ,  $l_{\text{cell}} = 2D$  being the periodicity of the array. We make use of the periodicity constraint on  $\beta$ ,  $\beta(z + l_{\text{cell}}) = \beta(z)$  and thus obtain:

$$M(z + l_{\text{cell}}|z) = \begin{pmatrix} \cos \Phi + \alpha \sin \Phi & \beta \sin \Phi \\ -\gamma \sin \Phi & \cos \Phi - \alpha \sin \Phi \end{pmatrix}, \quad (42)$$

where  $\gamma = (1 + \alpha^2)/\beta$  and  $\Phi = \psi(l_{\text{cell}})$  is the phase advance per unit cell. Since the integral in Eq. (38) is taken over a full period,  $\Phi$  is independent of  $z$ . The matrix in Eq. (42) is known as the Courant-Snyder matrix. We can now equate this matrix to the explicit form for the transfer matrix for one lattice unit, and so obtain  $\beta(z)$ . For example, at a distance  $z$  beyond the start of a focussing

lens,  $M(z + l_{\text{cell}}|z) = F(z).O(S).D(L).O(S).F(L - z)$ . We then obtain  $\Phi$  using the relation  $\cos \Phi = \text{Tr}(M)/2$ , and then find  $\beta$  by equating the upper right hand element of  $M$  to that of the Courant-Snyder matrix.

Figure 17(a) shows a few trajectories (dashed lines) calculated using Eq. (37) with  $\kappa L = 1$ ,  $\kappa S = 0.5$ , and arbitrarily chosen values for  $\epsilon_i$  and  $\delta_i$ . The motion is a product of two periodic functions, one of wavelength  $l_{\text{cell}}$  and the other of longer wavelength  $2\pi l_{\text{cell}}/\Phi$ . It is often the case that  $\Phi \ll 2\pi$ , in which case the modulation with wavelength  $l_{\text{cell}}$  has a small amplitude and is called the micromotion, while the much longer wavelength motion is called the macromotion. For the case shown in the figure,  $\Phi = 0.38\pi$  and the separation into a micromotion and a macromotion is evident. If we consider a large collection of molecules, all having different values of  $\delta_i$  and  $\epsilon_i$ , the only constraint being that every  $|\epsilon_i| < \epsilon$ , then all the trajectories will be bounded by the envelope  $\pm\sqrt{\beta\epsilon}$ . The bold lines in the figure show this envelope. The figure shows that the beam size modulates with the period of the array, reaching its maximum size in the centre of every focussing lens, and its minimum size in the centre of every defocussing lens. Since the confining and deconfining forces are linear in the off-axis displacements, the defocussing lenses have less effect on the beam than the focussing lenses, this being the key to the stability of the alternating gradient array. As the power of the lenses increases, so too does the depth of modulation of the envelope until, at the stability boundary where  $\Phi = \pi$ , the beam size becomes zero at the centre of the defocussing lens.

Using the first line of Eq. (37) and its derivative to form the quantity  $x^2 + (\alpha x + \beta v_x/\Omega)^2$ , we find the invariant

$$\gamma x^2 + 2\alpha x v_x/\Omega + \beta (v_x/\Omega)^2 = \epsilon_i. \quad (43)$$

This equation defines an ellipse in the phase-space whose coordinates are  $x$  and  $v_x/\Omega$ . The coordinates of all molecules with the same value of  $\epsilon_i$  but different values of  $\delta_i$  lie on this ellipse. Replacing  $\epsilon_i$  by  $\epsilon$  gives us the ellipse that bounds the entire set of molecules in the collection discussed above. The shape of this ellipse changes periodically with  $z$ , but its area is a constant,  $\pi\epsilon$ . Figure 17(b) shows the phase-space ellipse at various positions in the array. The beam is diverging as it enters the focussing lens. Inside this lens the ellipse rotates, reaching its maximal spatial extent at the lens centre where its principal axes are parallel to the coordinate axes. The ellipse continues to rotate so that it is converging at the exit of the focussing lens, and still converging as it enters the defocussing lens. At the centre of the defocussing lens, the spatial extent is minimized and the principal axes of the ellipse are again along the coordinate axes. The beam then starts to diverge again.

Molecules will only be transmitted if their trajectories do not take them outside the natural boundaries formed by the electrodes. The characteristic size-scale in the transverse direction is  $r_0$  and so to calculate the

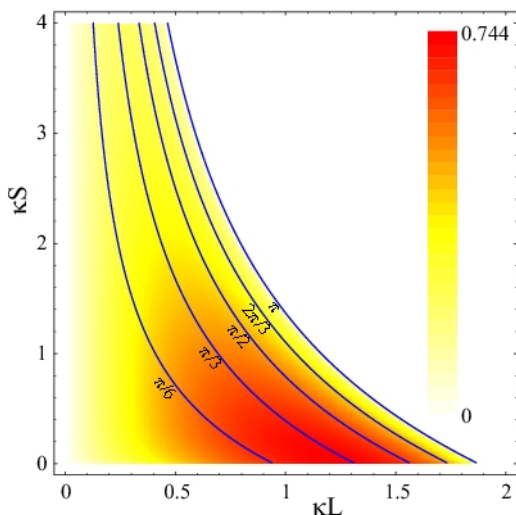


FIG. 18: Phase-space acceptance in one transverse direction, as a function of  $\kappa L$  and  $\kappa S$ . The acceptance is shown in units of  $\Omega r_0^2$ .

transverse phase space acceptance, we assume that the electrodes impose an aperture of size  $2r_0$  in each of the transverse directions. The beam characterized by  $\epsilon$  will be transmitted if  $\sqrt{\beta\epsilon} < r_0$  everywhere. In particular, the condition must be satisfied at the point where  $\beta$  has its maximum value,  $\beta_{\max}$ , which we already know is at the centre of every focussing lens. The phase space acceptance in  $(x, v_x)$  space is thus found to be  $\pi r_0^2 \Omega / \beta_{\max}$ . Figure 18 is a density plot of the phase-space acceptance in either transverse direction as a function of the two dimensionless parameters that define the array,  $\kappa L$  and  $\kappa S$ . The region of highest acceptance is found near  $\kappa L \sim 1, S \ll L$ , and the maximum value is  $0.744r_0^2\Omega$  obtained at  $\kappa L = 1.254, \kappa S = 0$ .

The requirement that  $\kappa L \sim 1$  for high acceptance constrains the aspect ratio of the lenses, i.e. the ratio  $L/r_0$ . Using Eq.(34) and setting  $\kappa L = 1$ , we obtain  $L/r_0 = \sqrt{N/\beta}$ . Typical values for a decelerator with a maximum field of 200 kV/cm are  $N = 80$  and  $\beta = 0.15$ , giving an aspect ratio of  $L/r_0 = 23.1$ . Since  $\kappa$  is inversely proportional to  $u$ , it will increase as the molecules slow down. To preserve the transverse acceptance, the lenses can be made progressively shorter so as to maintain  $\kappa L \sim 1$ . Alternatively, the alternating gradient array can have the structure  $(FO)^n(DO)^n$ , with the value of  $n$  decreasing down the beamline.

### E. Beyond the ideal model

In the previous section, we have used an idealized potential because it allows us to understand the main aspects of the dynamics in a straightforward way. This theoretical model misses some largely undesirable effects that are present in reality. In the transverse directions,

nonlinear forces are necessarily present and these reduce the transverse acceptance [57, 62]. The linear part of the force changes sign between one lens and the next, leading to the dynamical stability discussed above, but the leading order non-linear terms in the transverse force do not change sign between the focussing and defocussing lenses and so tend to upset the dynamical stability. Even when small compared to the linear terms, the non-linear terms can significantly reduce the transverse acceptance. Calculations for some typical electrode geometries are presented in [57]. In our idealized model, the axial and transverse potentials are completely decoupled. This cannot be achieved in any real decelerator because axial gradients of the electric field, needed for deceleration, change the dependence of the electric field on the transverse coordinates. In particular, the fringe fields at the ends of the lenses tend to increase the force constant in the defocussing direction relative to the one in the focussing direction, leading to further beam loss [57]. A realistic simulation of the transmission of molecules through an alternating gradient decelerator should use a three-dimensional map of the electric field magnitude produced by the electrode geometry of the machine, and the full electric-field dependence of the Stark shift. Simulations of this kind show that the true molecular trajectories in phase space are similar to those calculated with our simplified model, though the acceptance volume in phase space may be considerably smaller.

## VI. CONCLUDING REMARKS

In this chapter we have summarised how precise measurements on molecules are able to address important questions about the constancy of physical laws and the structure of fundamental interactions. This is a relatively new direction, which has emerged from a growing ability to prepare and manipulate molecules in pure quantum states. We have discussed the preparation of pulsed supersonic molecular beams and have explored how coherent control of the hyperfine levels can provide exquisite sensitivity to electric and magnetic fields. These same methods also provide an opportunity to search within molecules for more interesting effects, such as symmetry violations or variation of fundamental constants, which can be related to new physics on high energy scales. Deceleration and trapping are important for improving these experiments because they can increase the time available for coherent interaction with molecules from milli-seconds to seconds. Although we have focussed on decelerating heavy polar molecules using strong electric field seekers, the Stark deceleration method can also be applied to weak-field-seeking polar molecules and to Rydberg states of atoms and molecules. Alternatively, it is possible to decelerate and trap molecules using optical dipole forces. As methods for cooling, deceleration and trapping molecules reach ever lower temperatures and higher densities, and as they are extended to heavier and

to more diverse, molecules will surely play an increasingly important role in testing and understanding fundamental

physics.

- 
- [1] P. J. E. Peebles and Bharat Ratra, *Rev. Mod. Phys.* **75**, 559 (2003).
- [2] V. V. Flambaum and M. G. Kozlov, *Phys. Rev. Lett.* **99**, 150801 (2007).
- [3] Jean-Philippe Uzan, *Rev. Mod. Phys.* **75**, 403 (2003).
- [4] J. K. Webb, M. T. Murphy, V.V. Flambaum, V. A. Dzuba, J. D. Barrow, C.W. Churchill, J. X. Prochaska, and A. M. Wolfe, *Phys. Rev. Lett.* **87**, 091301 (2001); P. Tzanavaris, J. K. Webb, M. T. Murphy, V.V. Flambaum, and S. J. Curran, *Phys. Rev. Lett.* **95** 041301 (2005).
- [5] E. Reinhold, R. Buning, U. Hollenstein, A. Ivanchik, P. Petitjean, and W. Ubachs, *Phys. Rev. Lett.* **96**, 151101 (2006).
- [6] R. Srianand, H. Chand, P. Petitjean, and B. Aracil, *Phys. Rev. Lett.* **92**, 121302 (2004).
- [7] N. Kanekar, *et al.*, *Phys. Rev. Lett.* **95**, 261301 (2005).
- [8] Eric R. Hudson, H. J. Lewandowski, Brian C. Sawyer, and Jun Ye, *Phys. Rev. Lett.* **96**, 143004 (2006).
- [9] Brian C. Sawyer, Benjamin L. Lev, Eric R. Hudson, Benjamin K. Stuhl, Manuel Lara, John L. Bohn, and Jun Ye, *Phys. Rev. Lett.* **98**, 253002 (2007).
- [10] V.V. Flambaum and M. G. Kozlov, *Phys. Rev. Lett.* **98**, 240801 (2007).
- [11] R. Holzwarth, Th. Udem, T. W. Hänsch, J. C. Knight, W. J. Wadsworth, and P. St. J. Russell, *Phys. Rev. Lett.* **85**, 2264 (2000).
- [12] C. Daussy *et al.*, *Phys. Rev. Lett.* **94**, 203904 (2005).
- [13] S. Schiller and V. Korobov, *Phys. Rev. A* **71**, 032505 (2005).
- [14] J. van Veldhoven, J. Küpper, H. L. Bethlem, B. Sartakov, A. J. A. van Rooij, and G. Meijer, *Eur. Phys. J. D* **31**, 337 (2004).
- [15] Anne Amy-Klein, Andrei Goncharov, Mickal Guinet, Christophe Daussy, Olivier Lopez, Alexander Shelkovich, and Christian Chardonnet, *Opt. Lett.* **30**, 3320 (2005).
- [16] C. S. Wu, E. Ambler, R. W. Hayward, D. D. Hoppes and R. P. Hudson, *Phys. Rev.* **105**, 1413 (1957).
- [17] J. H. Christenson, J. W. Cronin, V. L. Fitch, and R. Turlay, *Phys. Rev. Lett.* **13**, 138 (1964).
- [18] L. I. Schiff, *Phys. Rev.* **132**, 2194 (1963); Eugene D. Commins, J. David Jackson, David P. DeMille, *Am. J. Phys.* **75**, 532 (2007).
- [19] P. G. H. Sandars, *Phys. Lett.* **14**, 194 (1965).
- [20] P. G. H. Sandars in *Atomic Physics 4* ed. G. zu Putlitz, (Plenum, 1975) p.71; O.P. Sushkov and V.V. Flambaum *Zh. Eksp. Teor. Fiz.* **75**, 1208 (1978).
- [21] D. Cho, K. Sangster, and E. A. Hinds, *Phys. Rev. Lett.* **63**, 2559 (1989); D. Cho, K. Sangster, and E. A. Hinds, *Phys. Rev. A* **44**, 2783 (1991).
- [22] C. A. Baker *et al.*, *Phys. Rev. Lett.* **97**, 131801 (2006).
- [23] M. V. Romalis, W. C. Griffith, J. P. Jacobs, and E. N. Fortson, *Phys. Rev. Lett.* **86**, 002505 (2001).
- [24] B. C. Regan *et al.*, *Phys. Rev. Lett.* **88**, 071805 (2002).
- [25] M. G. Kozlov and V. F. Ezhov, *Phys. Rev.* **A49**, 4502 (1994); M. G. Kozlov, *J. Phys. B* **30** L607 (1997); A. V. Titov, N. S. Mosyagin, V. F. Ezhov, *Phys. Rev. Lett.* **77** 5346 (1996); H. M. Quiney, H. Skaane, I. P. Grant, *J. Phys. B* **31** L85 (1998)(after correcting for the trivial factor of 2 between  $s$  and  $\sigma$  their result becomes 26 GV/cm); F. A. Parpia, *J. Phys. B* **31** 1409 (1998); N. Mosyagin, M. Kozlov, A. Titov, *J. Phys. B* **31** L763 (1998).
- [26] J. J. Hudson *et al.*, *Phys. Rev. Lett.* **89**, 023003 (2002). B. E. Sauer, H. T. Ashworth, J. J. Hudson, M. R. Tarbutt, and E. A. Hinds, in *Atomic Physics 20*, edited by Christian Roos, Hartmut Haeflner, and Rainer Blatt, AIP Conf. Proc. No. 869, (AIP, Melville, NY, 2006), p. 44.
- [27] D. DeMille *et al.*, in *Art and Symmetry in Experimental Physics*, AIP Conf. Proc. No. 596 (AIP, Melville, NY, 2001), pp. 7283; M. G. Kozlov and D. DeMille, *Phys. Rev. Lett.* **89**, 133001 (2002).
- [28] R. P. Stutz and E. A. Cornell, *Bull. Am. Soc. Phys.* **89**, 76 (2004); E. R. Meyer, J. L. Bohn, M. P. Deskevich, *Phys. Rev. A* **73**, 062108 (2006).
- [29] M. G. Kozlov and A. Derevianko, *Phys. Rev. Lett.* **97**, 063001 (2006).
- [30] S. C. Bennett and C. E. Wieman, *Phys. Rev. Lett.* **82**, 2484 (1999); R. D. Young, R. D. Carlini, A. W. Thomas, and J. Roche, *Phys. Rev. Lett.* **99**, 122003 (2007).
- [31] M. Quack, *Angew. Chem. Int. Ed.* **41**, 4618 (2002).
- [32] P. G. H. Sandars, *Origins of Life and Evolution of the Biosphere* **33**, 575 (2003).
- [33] Peter Schwerdtfeger, Jon K. Laerdahl, Christian Chardonnet, *Phys. Rev. A* **65**, 042508 (2002).
- [34] M. Ziskind, C. Daussy, T. Marrel, and Ch. Chardonnet, *Eur. Phys. J. D* **20**, 219 (2002).
- [35] P. Schwerdtfeger and R. Bast, *J. Am. Chem. Soc.* **126**, 1652 (2004).
- [36] D. DeMille, S. B. Cahn, D. Murphree, D. A. Rahmlow and M. G. Kozlov, *Phys. Rev. Lett.* **100**, 023003 (2008).
- [37] D. Colladay and V. A. Kostelecký, *Phys. Rev. D* **55**, 6760 (1997); **58**, 116002 (1998).
- [38] V. A. Kostelecký and C. D. Lane, *Phys. Rev. D* **60**, 116010 (1999).
- [39] Holger Müller, Sven Herrmann, Alejandro Saenz, Achim Peters, and Claus Lämmerzahl, *Phys. Rev. D*, **70**, 076004 (2004).
- [40] D. Colladay and V. A. Kostelecky, *Phys. Rev. D* **55**, 6760 (1997); *ibid.* **58**, 116002 (1998).
- [41] *Atomic and molecular beam methods*, edited by G. Scoles (Oxford University Press, Oxford, UK, 1988).
- [42] *Atomic and molecular beams: The state of the art 2000*, edited by R. Campargue (Springer, Berlin, 2001)
- [43] W. R. Gentry and C. F. Giese, *Rev. Sci. Instrum.* **49** (1978).
- [44] W. R. Gentry in *Atomic and molecular beam methods*, edited by G. Scoles (Oxford University Press, Oxford, UK, 1988).
- [45] D. E. Powers, S. G. Hansen, M. E. Geusic, A. C. Pulu, J. B. Hopkins, T. G. Dietz, M. A. Duncan, P. R. R. Langridge-Smith and R. E. Smalley, *J. Phys. Chem.* **86**, 2556 (1982).
- [46] M. R. Tarbutt, J. J. Hudson, B. E. Sauer, E. A. Hinds,

- V. A. Ryzhov, V. L. Ryabov and V. F. Ezhov, J. Phys. B **35**, 5013 (2002).
- [47] S. K. Tokunaga, J. O. Stack, J. J. Hudson, B. E. Sauer, E. A. Hinds and M. R. Tarbutt, J. Chem. Phys., **126**, 124314 (2007).
- [48] To produce short pulses, we apply voltage pulses of duration 150-300  $\mu$ s and of amplitude 200-350 V to a commercial solenoid valve (General Valve, Series 99, 50  $\Omega$ ).
- [49] B. E. Sauer, Jun Wang, and E. A. Hinds, J. Chem Phys. **105** 7412 (1996).
- [50] *Molecular Beams* N. F. Ramsey, (Oxford University Press, Oxford 1990).
- [51] J. J. Hudson, H. T. Ashworth, D. M. Kara, M. R. Tarbutt, B. E. Sauer, and E. A. Hinds, Phys. Rev. A. **76**, 033410 (2007).
- [52] H. L. Bethlem, G. Berden and G. Meijer, Phys. Rev. Lett. **83**, 1558 (1999).
- [53] S. Y. T. van de Meerakker, N. Vanhaecke, M. P. J. van der Loo, G. C. Groenenboom and G. Meijer, Phys. Rev. Lett. **95**, 013003 (2005).
- [54] S. Hoekstra, J. J. Gilijamse, B. Sartakov, N. Vanhaecke, L. Scharfenberg, S. Y. T. van de Meerakker and G. Meijer, Phys. Rev. Lett. **98**, 133001 (2007).
- [55] S. E. Maxwell, N. Brahms, R. deCarvalho, D. R. Glenn, J. S. Helton, S. V. Nguyen, D. Patterson, J. Petricka, D. DeMille and J. M. Doyle, Phys. Rev. Lett. **95**, 173201 (2005).
- [56] D. Patterson and J. M. Doyle, J. Chem. Phys. **126**, 154307 (2007).
- [57] H. L. Bethlem, M. R. Tarbutt, J. Küpper, D. Carty, K. Wohlfart, E. A. Hinds and G. Meijer, J. Phys. B **39**, R236 (2006).
- [58] H. L. Bethlem, A. J. A van Roij, R. T. Jongma and G. Meijer, Phys. Rev. Lett. **88**, 133003 (2002).
- [59] M. R. Tarbutt, H. L. Bethlem, J. J. Hudson, V. L. Ryabov, V. A. Ryzhov, B. E. Sauer, G. Meijer, and E. A. Hinds, Phys. Rev. Lett. **92**, 173002 (2004).
- [60] S. Y. Lee, Accelerator Physics (World Scientific, Singapore), (1999).
- [61] E. D. Courant and H. S. Snyder, Ann. Phys. **3**, 1 (1958). Reprinted in Ann. Phys. **281**, 360 (2000).
- [62] J. Kalnins, G. Lambertson and H. Gould, Rev. Sci. Instr. **73**, 2557 (2002).